

Water vapor induced self-assembly of islands/honeycomb structure by secondary phase separation in polystyrene solution with bimodal molecular weight distribution

Maciej Łojkowski, Adrian Chlanda, Emilia Choińska, Wojciech Swieszkowski

Submitted date: 05/05/2021 • Posted date: 07/05/2021

Licence: CC BY-NC-ND 4.0

Citation information: Łojkowski, Maciej; Chlanda, Adrian; Choińska, Emilia; Swieszkowski, Wojciech (2021):

Water vapor induced self-assembly of islands/honeycomb structure by secondary phase separation in polystyrene solution with bimodal molecular weight distribution. ChemRxiv. Preprint.

<https://doi.org/10.26434/chemrxiv.14054033.v7>

The formation of complex structures in thin films is of interest in many fields. Segregation of polymer chains of different molecular weights is a well-known process. However, here, polystyrene with bimodal molecular weight distribution, but no additional chemical modification was used. It was proven that at certain conditions, the phase separation occurred between two fractions of bimodal polystyrene/methyl ethyl ketone solution. The films were prepared by spin-coating, and the segregation between polystyrene phases was investigated by force spectroscopy. Next, water vapour induced secondary phase separation was investigated. The introduction of moist airflow induced the self-assembly of the lower molecular weight into islands and the heavier fraction into a honeycomb. As a result, an easy, fast, and effective method of obtaining island/honeycomb morphologies was demonstrated. The possible mechanisms of the formation of such structures were discussed.

File list (3)

Masło w masle_May21.pdf (1.98 MiB)

[view on ChemRxiv](#) • [download file](#)

TOC.tiff (1.65 MiB)

[view on ChemRxiv](#) • [download file](#)

Supporting_information_may21.pdf (1.85 MiB)

[view on ChemRxiv](#) • [download file](#)

1 **Water vapor induced self-assembly of islands/honeycomb structure by secondary phase**
2 **separation in polystyrene solution with bimodal molecular weight distribution**

3 Authors: Maciej Łojkowski^{1,*}, Adrian Chlanda^{1,2}, Emilia Choińska¹, Wojciech
4 Swieszkowski^{1*}.

5 Affiliation:

6 1. Faculty of Material Sciences and Engineering, Warsaw University of Technology,
7 Wołoska 141, 02-507 Warsaw, Poland

8 2. Department of Chemical Synthesis and Flake Graphene, Łukasiewicz Research
9 Network - Institute of Microelectronics and Photonics, Aleja Lotników 32/46, 02-
10 668 Warsaw, Poland.

11 **Abstract**

12 The formation of complex structures in thin films is of interest in many fields. Segregation of
13 polymer chains of different molecular weights is a well-known process. However, here,
14 polystyrene with bimodal molecular weight distribution, but no additional chemical
15 modification was used. It was proven that at certain conditions, the phase separation occurred
16 between two fractions of bimodal polystyrene/methyl ethyl ketone solution. The films were
17 prepared by spin-coating, and the segregation between polystyrene phases was investigated by
18 force spectroscopy. Next, water vapour induced secondary phase separation was investigated.
19 The introduction of moist airflow induced the self-assembly of the lower molecular weight into
20 islands and the heavier fraction into a honeycomb. As a result, an easy, fast, and effective
21 method of obtaining island/honeycomb morphologies was demonstrated. The possible
22 mechanisms of the formation of such structures were discussed.

23

24 **Keywords**

25 self-assembly; polymer thin films; bimodal molecular weight distribution; polystyrene; spin-
26 coating; honeycomb; breath figures; liquid-liquid phase separation; viscoelastic phase
27 separation; secondary quench;

28

29 **Introduction**

30 Complex morphologies comprising micro-islands and especially micropillars have gained
31 attention due to their wide range of possible applications, such as their special wetting
32 properties (1,2), application in studying biofilm formation (3), or controlling stem cell
33 differentiation (4). Two widespread methods that allow the creation of a broad range of
34 structures of polymer thin films (PTFs) are spin-coating (5) and breath figures (6). These
35 methods were applied for manufacturing organic ferroelectric switches (7), light-emitting
36 devices (8), sensors (9,10), drug delivery systems (11,12), biologically active surfaces (13,14),
37 functional nanostructured surfaces (15,16), and membranes (17). These processes rely heavily
38 on the interaction dynamics between the solvent, the polymer, and the vapours in the vicinity
39 of the surface. During spin-coating, a droplet of a mixture of a solvent and one or two polymers
40 is dropped onto the substrate. Subsequently, the substrate is rotated very quickly to cover it
41 uniformly with the solution's liquid film. As a result, the solvent evaporates. Thus, solvent and
42 temperature quench occurs. The spin coating can be divided into time regions. First, the liquid
43 solution droplet is spread hydrodynamically over the substrate. This regime is often referred to
44 as hydrodynamic thinning. Later, when a flat layer of the solution was obtained, the evaporation
45 of the solvent was responsible for further thinning of this layer.(18) Changes in the solvent
46 volume fraction and temperature often lead to unintentional or intentional liquid-liquid phase
47 separation.(19) It has been argued that such phase separation often starts in the early stages of
48 the regime controlled by evaporation.(19,20) Further spinning of the solution leads to gel
49 formation, which eventually slows down the diffusion inside the film. As a result, the

50 morphology becomes frozen in time before reaching equilibrium. The time necessary for the
51 morphology to stop evolving depended on the solvent evaporation rate, solution viscosity,
52 spinning rate, and substrate thermal properties.(21–23) During coating formation, a range of
53 events attributed to the local thermal instabilities takes place: heat transfer between the bottom
54 and top layers of the film; heat transfer from the air above the layer; heating the substrate by
55 the surrounding air; and local lateral temperature variance due to the thermal conductivity and
56 heat capacity of the substrate.(23) These events may lead to the unnecessary or intended
57 waviness of the coating profile. This undulation is often attributed to two interconnected
58 phenomena. One is the flow of the liquid due to thermal convection. The second is the surface
59 tension gradient due to local composition differences, which manifests in solvent-rich or
60 solvent-depleted areas.(18) The solvent-depleted areas have higher surface tension and thus
61 pull the liquid towards these areas and up, while the solvent-rich areas sink, forming valleys.
62 High centrifugal force during spin-coating is often a cause of elongation of the mentioned
63 structures. As a result, long stripes extending from the centre of the sample are observed. Using
64 solvents with low surface tension, the addition of a surfactant or using a mixture of solvents
65 can suppress the formation of these features. Furthermore, decreasing the amount of heat can
66 suppress the formation of convection cells and allow smooth coating preparation.

67 In the second technique mentioned above, breath figures appear on the liquid film's surface
68 when the humid airflow accelerates the evaporation rate. Successively, the temperature
69 decreases, which results in nucleation and growth of water droplets. These droplets create a
70 regular honeycomb array of cavities in the film. The temperature increased to that of the
71 surroundings, and the droplets evaporated, leaving a porous surface. After most of the solvent
72 had evaporated, the start of droplet nucleation was governed by the onset time related to the
73 solvent evaporation rate, solution concentration, and airflow.(24)

74 The location and width of the MWD can affect solid thin polymeric film formation to achieve
75 unique properties (25). Wu et al. studied the effect of MWD on the self-assembly of end-
76 functionalized polystyrenes. They proposed a new way of controlling the morphology of PTF
77 obtained via breath figures by changing the MWD width. As a result, a porous membrane with
78 higher robustness was obtained.(26) The width of the MWD can be tailored either within the
79 polymerization process (27,28) or by mixing two polymer species with a very narrow MWD
80 (29). Heitmiller et al. reported that a heterogeneous melt of polyethylene had a higher flow
81 index than a homogeneous melt.(30) The investigation performed by Koningsveld et al. has
82 shown that the bimodal MWD has a significant effect on the liquid-liquid binodal curve of
83 polymers in solution.(31) Phase regions characterise such solutions, and liquid-liquid phase
84 separation between polymer- and solvent-rich fractions can occur. Zeman et al. demonstrated
85 that the critical concentration enabling phase separation in a solution of two polymer species
86 decreases with an increase in the molecular weight M_w .(32) Moreover, even when the polymer-
87 polymer interactions are athermal, i.e. Flory-Huggins interaction parameter χ equals zero, and
88 phase separation can occur due to the large difference in entropy between long and short chains,
89 which act as separate entities and influence the viscosity of bimodal solutions.(33) The
90 evaporation of the solvent followed by temperature quenching can be responsible for phase
91 separation, as the Flory-Huggins parameter is temperature dependent and decreases with
92 temperature. The quenched mixture can turn from the one-phase state to an unstable state.
93 Interestingly, Henderson et al. investigated a two-step process in which the first temperature
94 quench forces phase separation and the spinodal structures are allowed to coarsen; next, even
95 deeper quenching is enacted.(34) This two-step quench led to the formation of small well-
96 dispersed domains within the primary domains. Intriguingly, the combined spin-coating and
97 breath figure methods would lead to two quenching and heating events. First, solvent
98 evaporation would decrease the temperature. Second, water condensation would increase the

99 temperature, and finally, evaporating water would again decrease the temperature. Another
100 interesting theory is “viscoelastic phase separation”. Phase separation occurs due to an
101 imbalance of the viscoelastic properties of the components.(35) Polymer melts with bimodal
102 molecular weights show nonlinear rheology. A rheological investigation by Hengeller et al.
103 reported two regimes of stress relaxation in such a melt, where either the only short or only
104 long chains underwent stress relaxation, depending on the time scale.(36) Harris et al. found
105 that the viscosity of the blend of bimodal polystyrene can be considered a sum of
106 components.(37) It has been discussed that blending polystyrenes with different molecular
107 weights mixed the entanglement types between polymer chains. The polymer concentration in
108 the solvent changes how the polymer chains interact. Two polymer chains act as separate
109 entities, provided that the concentration is below the overlap concentration (C^*). However, once
110 the overlap concentration occurs, the polymer's cooperative motion starts, and the behaviour of
111 the solution changes.(38,39)

112 Successive research has focused on studying how polymer chains of varying lengths segregate
113 in PTFs. Hariharan et al. investigated the effect of the entropy of spin-coated and annealed
114 bimodal PTFs on polymer chain segregation.(40) It was shown that higher entropy of shorter
115 chains led to their segregation on the PTF surface, while the longer chains' lower entropy
116 promoted their segregation in bulk. Tanaka et al., in turn, studied spin-coated polystyrene
117 blends with low and high M_w with narrow MWD utilizing toluene as a solvent. They reported
118 that PTFs consisting of polystyrenes with a low molecular weight demonstrated surface
119 segregation after thermal treatment.(29) Several other recent studies have illustrated the
120 segregation of lower molecular mass elements towards the surface during annealing.(41–45)

121 On the other hand, it has been shown that deuterated polymer segregation can change the
122 surface roughness after annealing the coating.(46–49)

123 In the present study, to modify the coating morphology, we decided to explore the phase
124 separation between two kinds of polystyrene with low and high molecular weights mixed in a
125 solvent. We changed the polydispersity, and we used uniform polystyrene standards as a
126 reference. The solvent methyl ethyl ketone MEK was chosen because of its suitability for spin-
127 coating.⁽⁵⁰⁾ However, for most, its hygroscopic properties, as we planned to perform spin-
128 coating in humid conditions. MEK is considered a marginal solvent for PS, while it is more
129 hygroscopic than typically used solvents for polystyrene.^(51,52)

130 For our study, we established the following assumptions. The mixture with sufficiently high
131 polydispersity will phase separate during spin-coating, even if these species are chemically
132 identical. The study will be performed in the regime where thermocapillary effects cause
133 undulations to make any morphological changes clearer to observe. The breath figure technique
134 will be combined with spin-coating to induce additional motion caused by the surface tension
135 of water.

136 The study is organized in the following order. First, the effect of the bimodal weight distribution
137 on the viscosity of the solutions is discussed. Next, the morphology of the coatings spun at the
138 most negligible possible humidity is compared by analysis of atomic force microscopy and
139 optical microscopy images. Then, force spectroscopy was used to identify the different
140 polystyrene phases. In situ reflectometry was used to measure the evaporation time of the
141 solutions. Finally, the coatings spun at different humidity levels were investigated by optical
142 and atomic force microscopy.

143 It was found that at a relative humidity of 75%, a solution concentration of 80 mg/ml and
144 polystyrene molecular weights of 20 kDa and 200 kDa mixed in a 75/25 w/w% ratio, the two
145 phases formed islands (lower M_w fraction) embedded inside of the honeycomb (higher M_w
146 fraction).

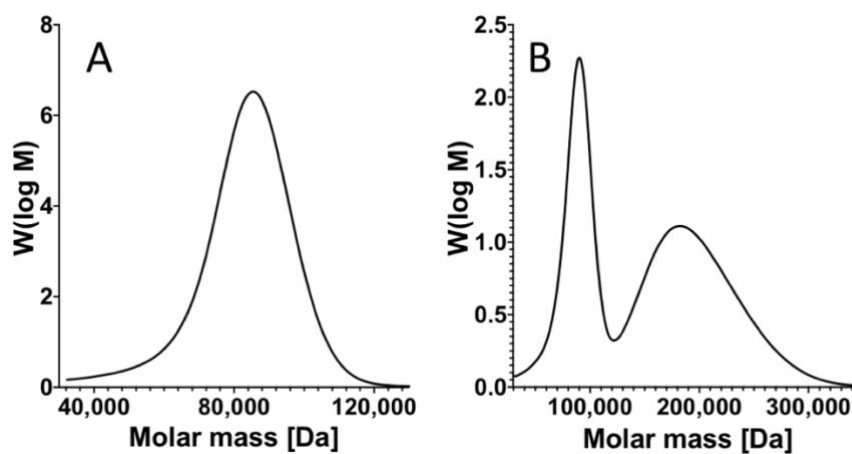
147 Although spin-coating was chosen for its ease of controlling the evaporation rate, we believe
148 that the proposed method can be extended to other techniques, such as dip-coating or ink-jet
149 printing. The presented results can also be treated as a starting point for other interesting
150 experiments.

151

152 **Result and discussion**

153 The solutions with bimodal MWD were prepared so that the two nodes in the distribution were
154 clearly separated. The GPC molecular weight distribution of a single node MWD (uniform) is
155 presented in Fig. 1 A, which illustrates the MWD of 91 kDa polystyrene with a narrow
156 distribution (PDI=1.04). In contrast, Fig. 1 B illustrates the MWD with two nodes of a blend of
157 91 kDa PS with 200 kDa PS, both with narrow distributions (PDI=1.04).

158



159

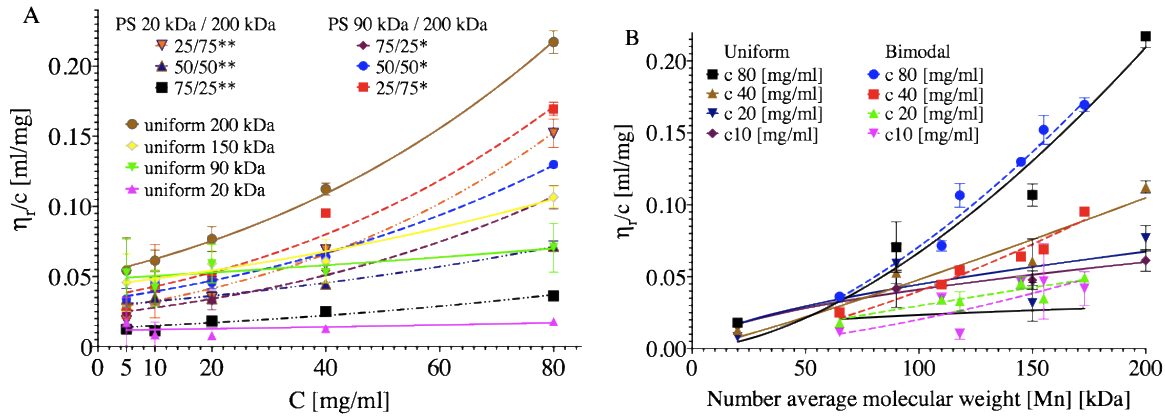
160 Fig 1. Exemplary GPC experiment results of bimodal and uniform MWD polystyrene; A -
161 narrow uniform MWD, $M_w = 91$ kDa, PDI 1.04; B – bimodal MWD, blend of $M_w = 91$ kDa,
162 PDI = 1.04 and $M_w = 200$ kDa, PDI = 1.04. (GraphPad Prism 9, <https://www.graphpad.com>)

163

164 • **Evaluation of solution viscosities**

165 The viscosity measurement (Fig. 2) can be used to assess not only the final coating thickness
166 and the solvent evaporation time prediction but also the characteristics of polymer chain

167 interactions. The measurement result is presented as reduced viscosity η_r/C , where C represents
 168 the concentration in mg/ml. Here, $\eta_r = \frac{\eta - \eta_s}{\eta_s}$, where η is the dynamic viscosity of the solution
 169 and η_s is the viscosity of the solvent. In Fig. 2A, the viscosity is plotted as a function of the
 170 concentration.
 171



172
 173 Fig. 2. Reduced viscosity η_r/C of the solutions, A - η_r/C plotted against the solution's
 174 concentration. Curves represent fits for eq. 2; B - η_r/C plotted as a function of the number
 175 average molecular weight function. Curves represent the Mark-Houwink equation fit (eq. 3),
 176 $[M_n] = f_1M_{w1} + f_2M_{w2}$, where f is w/w % ratio of polymers. (GraphPad Prism 9,
 177 <https://www.graphpad.com>)
 178

179 The general dependence of viscosity on concentration can be described in the form of a power
 180 series:(53)

$$181 \frac{\eta_r}{c} = [\eta] \left(1 + K[\eta]C + \frac{K[\eta]C^2}{2} + \frac{K[\eta]C^3}{6} \right) \quad (2)$$

182 where $[\eta]$ is the intrinsic viscosity at infinite dilution. The coefficients are summarised in Table
 183 S1 in SI. The intrinsic viscosity $[\eta]$ was lower for bimodal blends. The overlap concentration is
 184 defined as the concentration at which the polymer chains start to overlap with each other.(54)
 185 The overlap concentration was estimated according to $C^*=1/[\eta]$. The overlap concentration for

186 20 kDa was 83 mg/ml and for 200 kDa was 19 mg/ml. Notably, in the case of the 80 mg/ml
187 solution, the 20 kDa species were in the semidilute regime, while the 200 kDa species were in
188 the concentrated regime.

189 The viscosity of the bimodal solutions increased faster with increasing concentration than in
190 the case of uniform solutions. The K parameter was particularly high for 75/25 blends: 1.36 for
191 90 kDa and 200 kDa and 1.01 for 20 kDa and 200 kDa. In comparison, K for uniform 200 kDa
192 was 0.36. Thus, it can be assumed that the number of entanglements attributed to the 200 kDa
193 fraction rises at higher concentrations. Fig. 2B presents the viscosity in relation to the number
194 molecular weight $[M_n]$. The relation between viscosity and molecular weight can be described
195 in the form of the Mark-Houwink equation:(53)

$$196 \frac{\eta_r}{c} = \ln K + a \ln[M_n]. \quad (3)$$

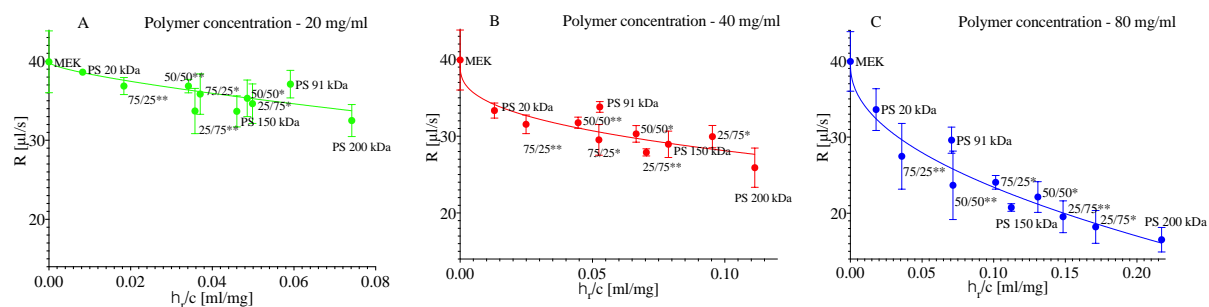
197 The K and $[\eta]$ values are summarised in SI, Table S2. The uniform solutions were visibly more
198 viscous than their bimodal counterparts of similar molecular weights at concentrations below
199 20 mg/ml. It could be expected that the bimodal solutions will change their behaviour more
200 severely when solvent evaporation would quench them towards more concentrated regimes.

201

202 • **Evaporation of the solvent during spin-coating**

203 As presented in Fig. 3, the evaporation rate R depends on the viscosity of the solutions. The
204 evaporation of the 20 kDa, 91 kDa and 200 kDa samples differs for the same concentration.
205 These differences became more transparent at a concentration of 80 mg/ml.

206



207
 208 Fig. 3. The relation between the evaporation rate of solution and the reduced viscosity of
 209 solution for polymer concentrations: A - 20 mg/ml, B - 40 mg/ml, and C - 80 mg/ml. The curves
 210 represent the Padé approximation trend line. (GraphPad Prism 9, <https://www.graphpad.com>)

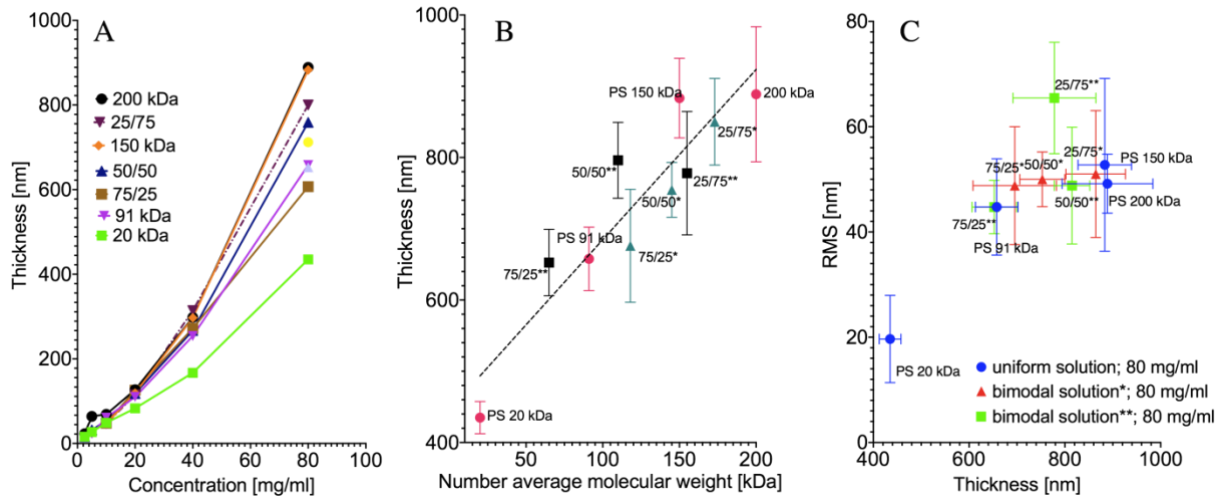
211
 212 • **Investigation of the thickness and morphology of the coatings spun at a relative**
 213 **humidity of 0%**

214 The coatings spun at Rh 0% were chosen as a starting point for the investigation. We decided
 215 to look for phase separation if no humidity was applied, affecting the investigated solvent-
 216 polymer system. The convection Marangoni flow, solvent evaporation, and phase separation
 217 events alter the coating surface morphology. As a result, the occurrence of wrinkles or arrays
 218 of islands on the coating surface was reported. (48,55–57)

219 The coatings were investigated via AFM and optical imaging to determine the effect of bimodal
 220 MWD on coating morphology. Significant differences between blend types occurred (Fig. 4A).

221 The solution concentration of 80 mg/ml was chosen. As we expected from the tests mentioned
 222 earlier, the bimodal distribution role would be the highest. Moreover, we wanted to avoid the
 223 influence of the substrate on our force spectroscopy experiment. For that, we needed the
 224 thickest coating. As illustrated in Fig. 4B, the thickness of the coatings in the case of 80 mg/ml
 225 scaled linearly with the blends' average molecular weight. No correlation between the thickness
 226 and roughness was found. (Fig. 4C).

227



228

229 Fig. 4. A - Thickness of the coatings with respect to the composition and the concentration. The
 230 plot presents data for uniform and 91 kDa/200 kDa solutions. B – Thickness of the coating for
 231 80 mg/ml concentration in the blend's molecular weight function. * - Blends of 91 kDa and 200
 232 kDa polystyrene; ** - blend of 20 kDa and 200 kDa polystyrene; x/x – w/w% ratio of blended
 233 homogeneous polystyrenes. The number average molecular weight $[M_n] = f_1M_{w1} + f_2M_{w2}$,
 234 where f w/w. % ratio of polymers. C - RMS roughness of the coatings spun from 80 mg/ml
 235 concentration. (GraphPad Prism 9, <https://www.graphpad.com>)

236

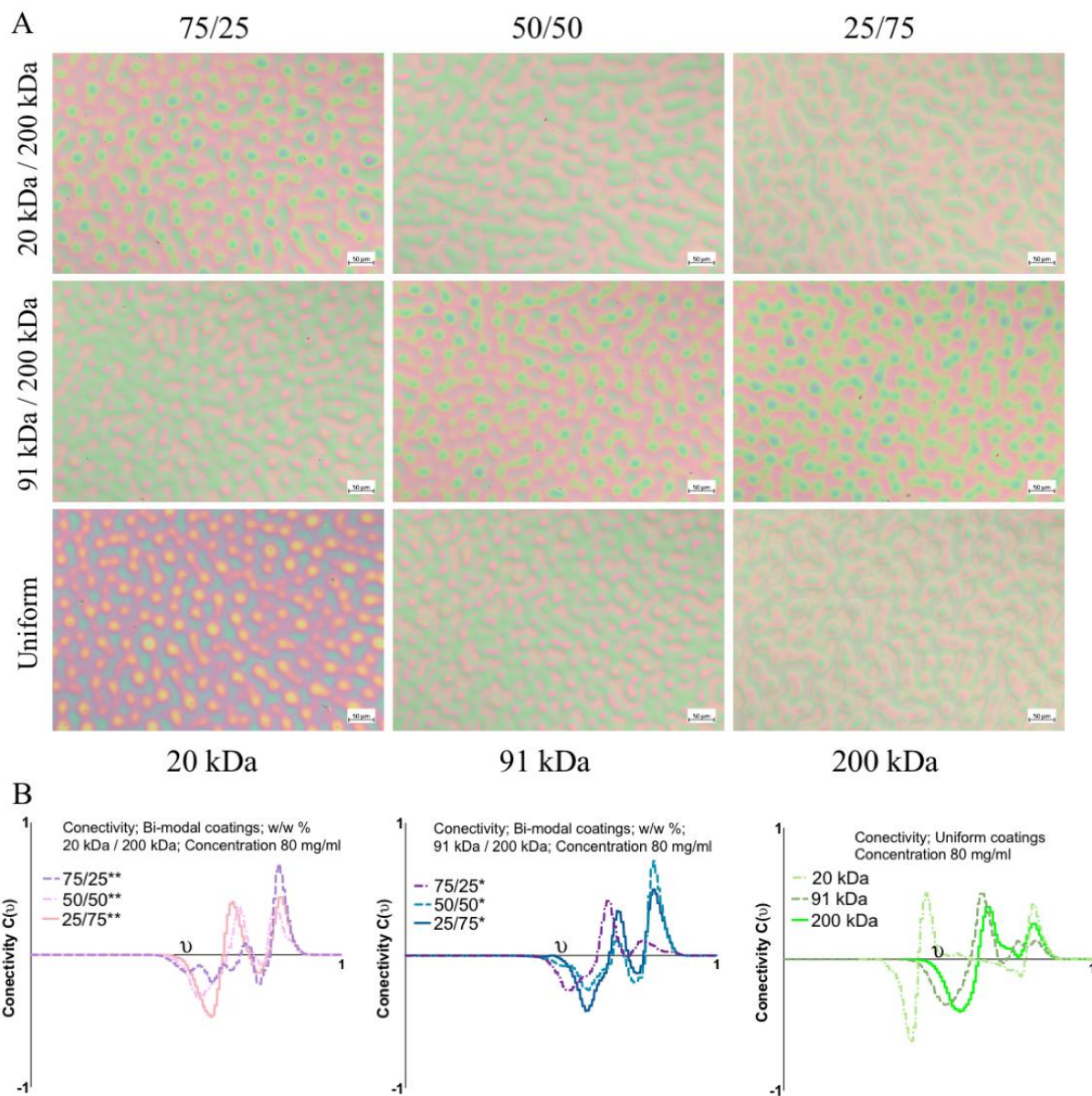
237 To represent the morphology of the material quantitatively, one can apply the Minkowski
 238 parameters.(58) The images (Fig. 5A) used for analysis come from the central part of the image
 239 to exclude the high shear rate effect on the coating morphology. The scale bar was 50 μ m.
 240 Based on this description, it can be concluded that the morphology of the uniform coatings is
 241 characterised by separate islands surrounded by a bicontinuous phase. In contrast, the bimodal
 242 coatings are characterised by a bicontinuous phase separated by interconnected islands.

243 Fig. 5B presents connectivity. Connectivity $C(\nu)$ can be used to describe the bicontinuous or
 244 island morphology of the coating with respect to the given binarization threshold ν . A negative
 245 value of connectivity corresponds to bicontinuous morphology, while a positive value
 246 corresponds to island morphology. The threshold was normalized to 1. Based on the

247 connectivity, the bimodal coatings had different morphologies than the uniform coatings when
248 the starting conditions (Rh 0%) were considered. With the exclusion of the 75/25 20 kDa 200
249 kDa coating, the coatings were characterized by peaks related to continuous structures and two
250 peaks related to islands.

251 In contrast, the uniform coatings had one set of continuous structures and two peaks related to
252 islands. In connection with the images, it can be assumed that these two kinds of islands are
253 one on top of another. In the case of bimodal blends, the presented situation describes a set of
254 interconnected islands on top of another interconnected structure.

255



256

257 Fig. 5. A - Optical images of coatings spun from 80 mg/ml. The B - Minkowski connectivity

258 $C(\nu)$ of the coatings spun from 80 mg/ml, where ν represents the threshold for image

259 binarization. The values on the axis were normalized to 1. (PowerPoint 365, GraphPad Prism

260 9, <https://www.graphpad.com>)

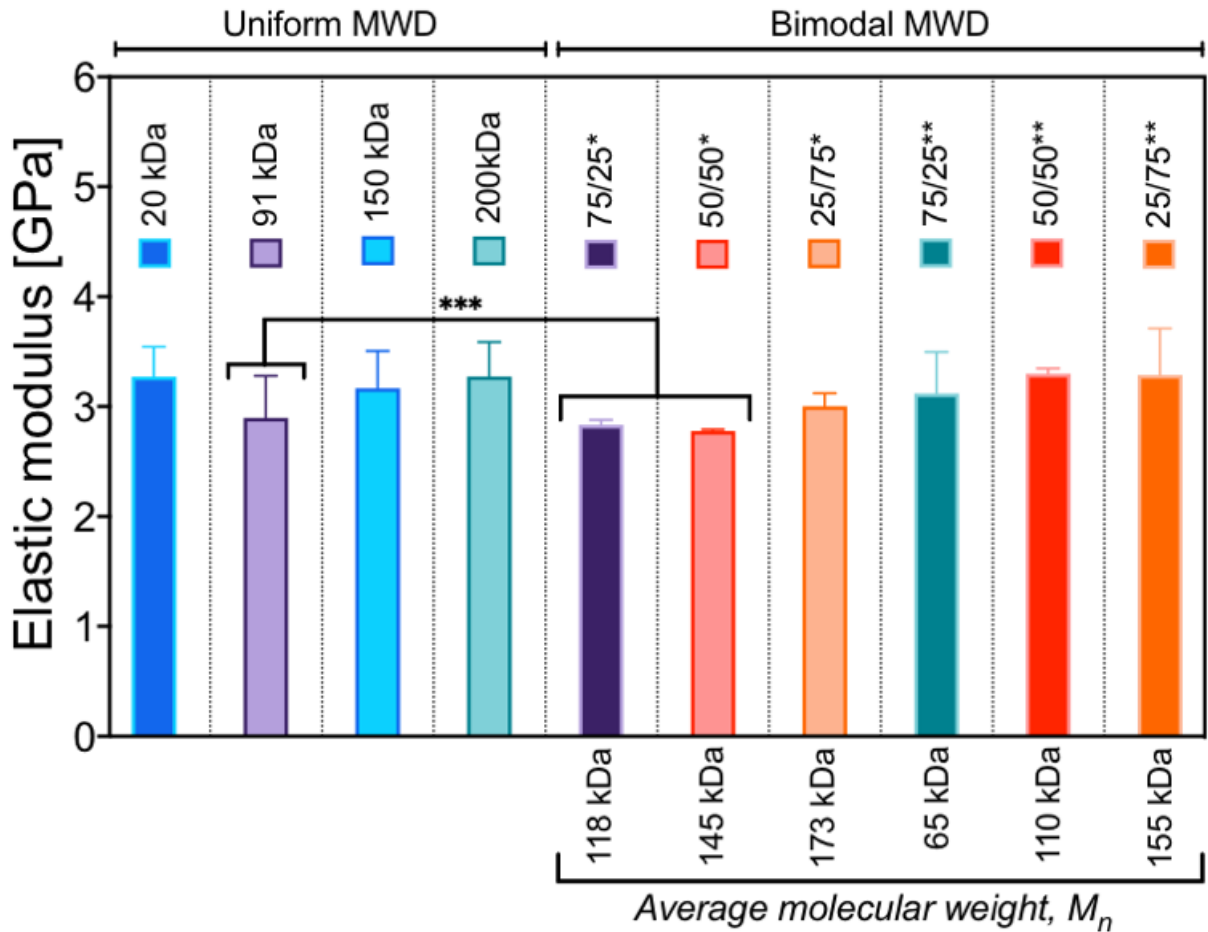
261

262 • **Investigation of coating phase composition by means of AFM force spectroscopy**

263 The AFM force spectroscopy method allows the visualization and quantification of surface

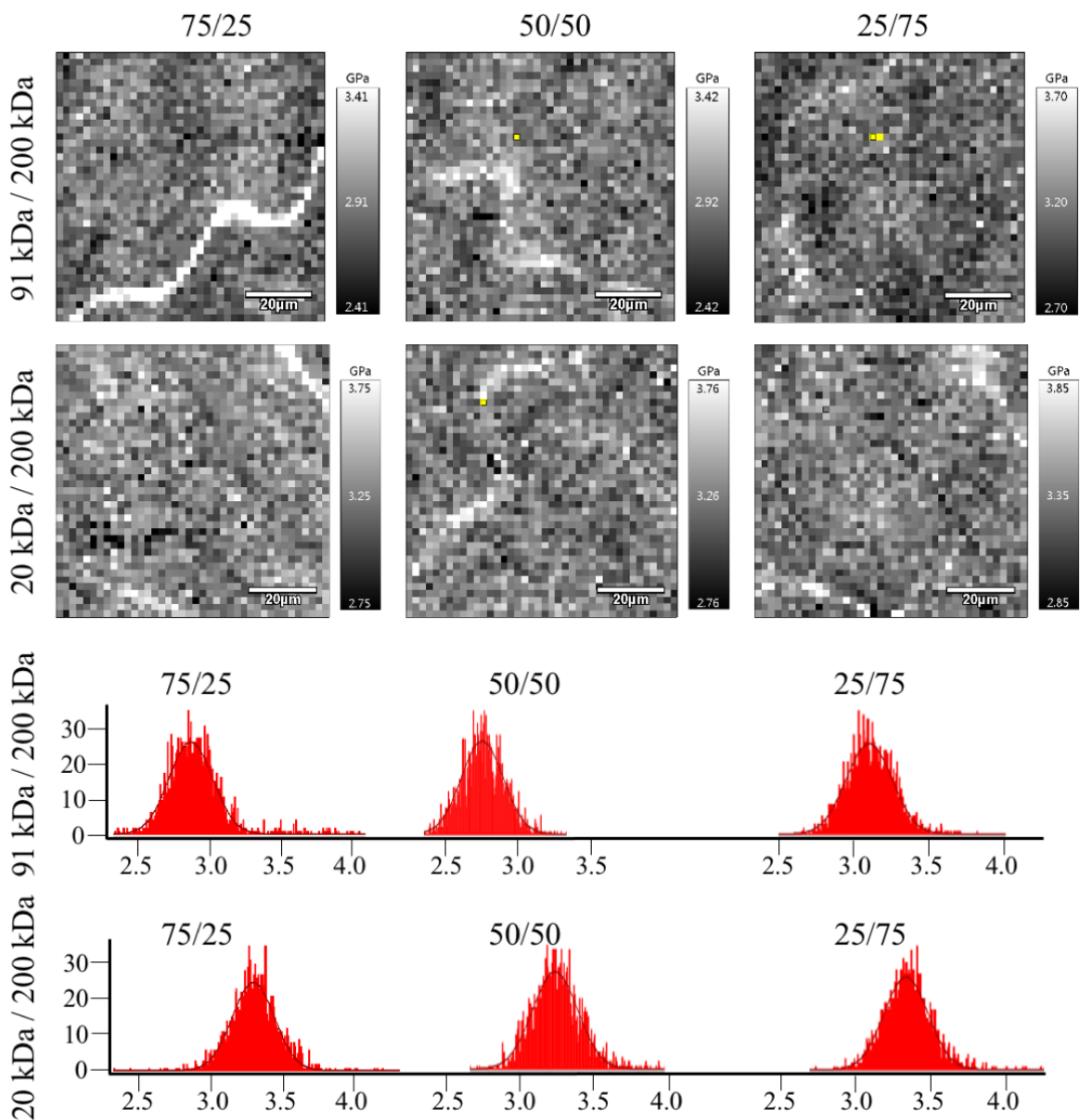
264 areas differing in mechanical properties.(59) The coatings spun from the solutions with 80

265 mg/ml concentration were studied. The resulting elastic modulus of the coatings was calculated
 266 (Fig. 6).
 267



268
 269 Fig. 6. Average elastic modulus obtained based on the FS method for coatings made from a
 270 solution of 80 mg/ml. Uniform – coatings were made from homogeneous solutions; bimodal –
 271 coatings made from solutions with bimodal MWD; * - blends of 91 kDa and 200 kDa
 272 polystyrene; ** - blend of 20 kDa and 200 kDa polystyrene; x/x – w/w% ratio of blended
 273 homogeneous polystyrenes. $[M_n] = f_1M_{w1} + f_2M_{w2}$, where f w/w % ratio of polymers. *** -
 274 means are significantly different (one-way ANOVA, $p < 0.05$). (GraphPad Prism 9,
 275 <https://www.graphpad.com>)
 276

277 The obtained results are similar to those found in the literature.(60) The uniform 91 kDa coating
278 and the 75/25 and 50/50 blends of 91 kDa and 200 kDa had significantly lower elastic moduli
279 than the rest of the tested groups. The dependence between the molecular weight and the elastic
280 modulus of the polymer has been repeatedly proven.(61,62) However, we did not find
281 significant differences between the other groups. The uniform 20 kDa coating had an elastic
282 modulus similar to that of the 200 kDa coating in our investigation. The 20 kDa coating was
283 the thinnest; thus, the substrate could influence the result. We performed a linear regression test
284 (SI, *Force Spectroscopy*, Fig. S4) between the thickness of the 80 mg/ml coatings and the elastic
285 modulus, which proved no relationship between the thickness of the coatings and the elastic
286 modulus, while the 20 kDa coating was an outlier (SI, *Force Spectroscopy*, Table S14).



287

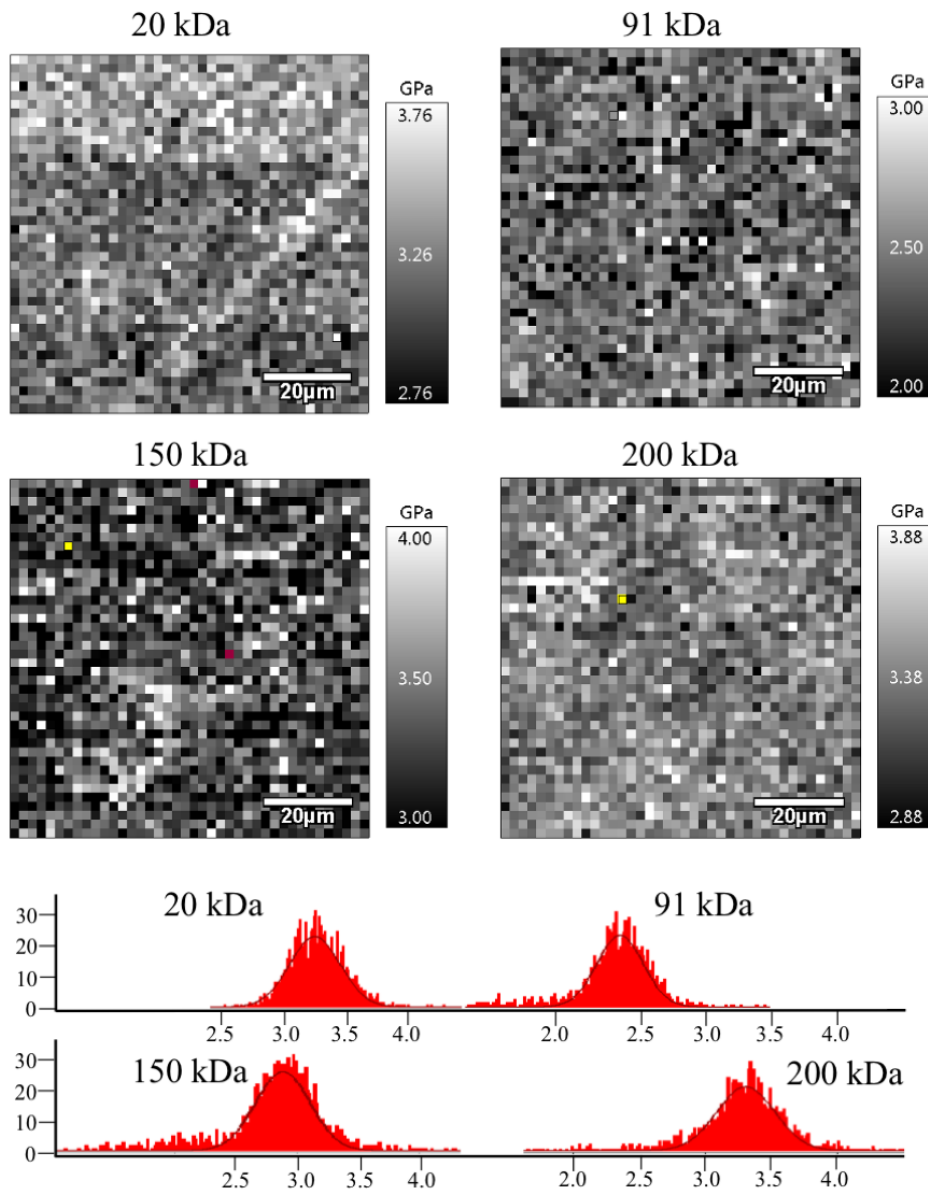
288 Fig. 7. Force spectroscopy maps of bimodal MWD coatings and corresponding histograms of
 289 the elastic modulus. The greyscale shows the stiffness – the white colour corresponds to the
 290 highest stiffness. The grayscale range is ± 1 GPa. (PowerPoint 365, Igor Pro 6.37 with Asylum
 291 Research 15.02.105 add-on, <https://afm.oxinst.com>)

292

293 Interestingly, it was possible to record local differences in the coating surface stiffness (Fig. 7).

294 The maps were gathered for bimodal coatings. White spinodal-like areas are characterized by

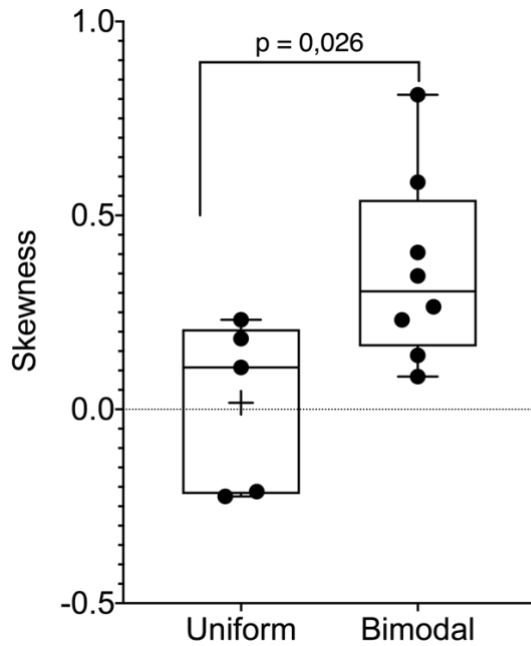
295 higher stiffness. The differences are more clearly visible in the case of 90 kDa and 200 kDa
296 blends, in agreement with Fig. 6.
297



298
299 Fig. 8. Force spectroscopy maps of coatings with uniform MWD and corresponding histograms
300 of the elastic modulus. The greyscale shows the stiffness – the white colour corresponds to the
301 highest stiffness. The grayscale range is ± 1 GPa. (PowerPoint 365, Igor Pro 6.37 with Asylum
302 Research 15.02.105 add-on, <https://afm.oxinst.com>)

303

304 For comparison, Fig. 8 illustrates the FS maps of the uniform coatings. We analysed the
305 skewness of the maps' elastic modulus distribution (SI, *Force Spectroscopy*, Table S15). The
306 skewness in the case of uniform coatings was significantly lower ($p < 0.05$) than that in the case
307 of bimodal coatings (Fig. 9). The distribution of the elastic modulus of the uniform coatings
308 was more homogeneous.



309 Fig 9. The skewness of the elastic modulus data sets. Uniform – grouped means that represents
310 the skewness of histograms of uniform coatings elastic modulus. Bimodal – grouped means that
311 represents the skewness of histograms of all kinds of bimodal blends elastic modulus. The
312 means of these two groups were significantly different ($p < 0.05$). (GraphPad Prism 9,
313 <https://www.graphpad.com>)
314

315

316 Therefore, it was concluded that force spectroscopy revealed phase separation in the bimodal
317 coatings. The most noteworthy phase separation was found for the 75/25 blends of both kinds
318 of bimodal coatings. Here, the phase of lower concentration formed long, spinodal-like forms.
319 For the 25/75 blends, the separate phases were scattered.

320

321 • **Solubility of polystyrenes with respect to the molecular weight distribution**

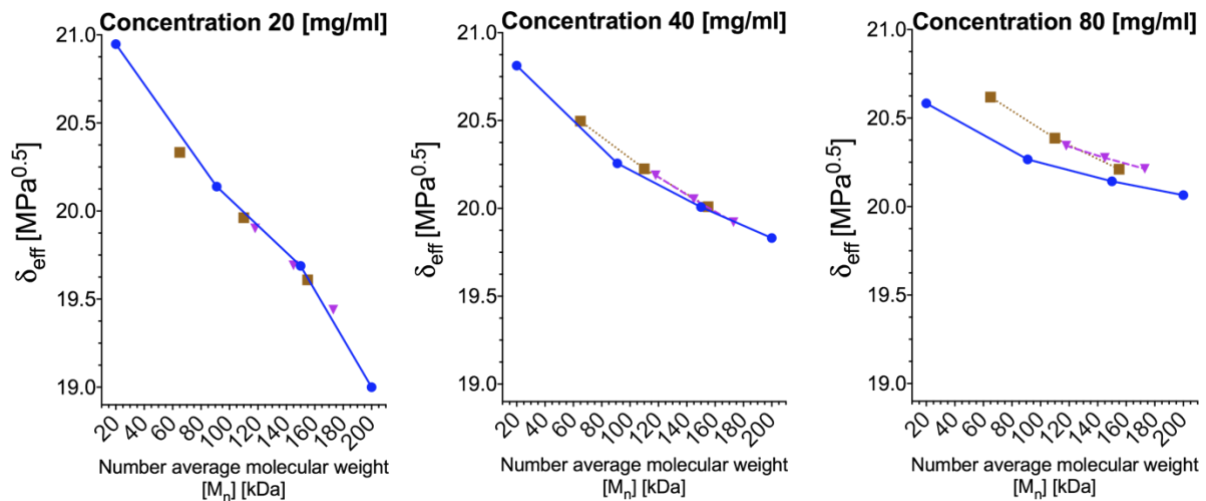
322 The phase separation mentioned above could be explained by solubility investigation. It was
323 shown that the viscosity of the polymeric solution could be utilised by the application of the
324 Mangaraj method to retract several polymer-solvent parameters, i.e. the Flory interaction
325 parameter.(63) We utilised the Mangaraj equation (eq. 4) to investigate the miscibility gap
326 between the lower- and higher-molecular-weight polystyrenes.(64)

327
$$\ln\left(\frac{\eta}{\eta_{max}}\right) = -(\delta_s - \delta_{eff})^2. \quad (4)$$

328 The effective miscibility parameter δ_{eff} was calculated with respect to a solution of 200 kDa
329 with a concentration of 80 mg/ml, which had the highest viscosity among the tested solutions
330 (η_{max}). The solvent δ_s was set to 19 MPa^{0.5}, which is a typical value for MEK.

331 The miscibility gap between low- and high-molecular-weight polystyrene can be derived based
332 on the PS blends' viscosity. Furthermore, the miscibility gap decreases accordingly with the
333 low molecular weight fraction. Here, δ_{eff} is the effective Hildebrand miscibility parameter
334 calculated based on the intrinsic viscosity $[\eta]$. For the 20 mg/ml concentration, all the solutions
335 are present on the same linear trend with the lowest δ_{eff} for the highest molecular weight. It
336 should be noted that with increasing concentration, the trends for 20 kDa/200 kDa solutions
337 (brown squares), 91 kDa/200 kDa solutions (purple triangles), and uniform solutions (blue
338 circles) become divergent at low molecular weights, with their trends coincident at 200 kDa
339 (Fig. 10).

340



341

342 Fig. 10. The effective miscibility parameter δ_{eff} of the polystyrenes in MEK with bimodal and
 343 uniform distributions for two kinds of bimodal distributions: 20 kDa/200 kDa – brown squares
 344 and 91 kDa/200 kDa – purple triangles; the blue circles represent data for polystyrenes with
 345 uniform distributions. $[M_n] = f_1M_{w1} + f_2M_{w2}$, where f w/w % ratio of polymers. (GraphPad Prism
 346 9, <https://www.graphpad.com>)

347

348 • **Self-assembly of micro islands/honeycombs due to phase separation and water**
 349 **condensation**

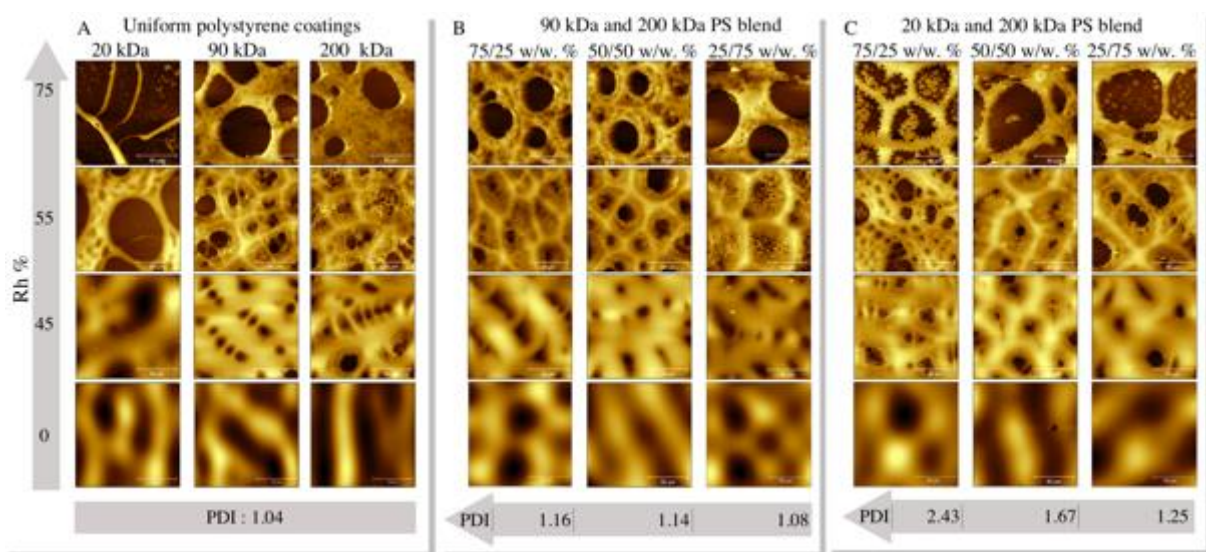
350 As a follow-up, we utilized humidity to take advantage of the phase separation observed above.
 351 It was assumed that phase separation could be further enhanced if spin-coating was performed
 352 under humid conditions. It was further concluded that water condensation would eventually
 353 lead to ruptures in the solution layer. By this, a new interface between the solution, water, and
 354 SiO₂ substrate would be created. This would induce separation between segregated phases. The
 355 condensing water forces the liquid film to dewet and retreat from SiO₂. The viscosity gradient
 356 between different phases would lead to the formation of convection cells and honeycomb
 357 morphology.(65,66) It was assumed that the spinodal-like structures found during the FS
 358 investigation, probably consisting of a higher molecular weight fraction, would reinforce the
 359 honeycomb borders. As revealed by the viscosity investigation, the longer polymer chains

360 would carry the stress as they would be highly entangled. The lower molecular phase would
 361 separate because no stress would be applied to the shorter chains. It should also be considered
 362 that MEK is a hygroscopic solvent, while PS is slightly hydrophobic. The absorption of water
 363 by MEK can further alter the interactions between the solvent and different PS phases. The
 364 viscosity and solubility investigations pointed to 80 mg/ml concentration to obtain the most
 365 pronounced effect. It was also assumed that water condensation would take place in the later
 366 stage of spinning. As the humidity slows evaporation, the highest humidity allows the longest
 367 time for morphology formation. The tested relative humidity Rh values were 45%, 55%, and
 368 75%.

369 Fig. 11 A shows images of coatings composed of uniform polystyrenes, Fig. 11 B presents
 370 images of coatings prepared from 91 kDa and 200 kDa blends, and Fig. 11 C presents images
 371 of coatings prepared from 20 kDa and 200 kDa blends.

372 Each column is marked below with the mixture's PDI value, and each row corresponds to one
 373 of the Rh values. Optical microscopy showing three different areas of the coatings is presented
 374 in the Supplementary Information, Figs. S6 – S8.

375



376

377 Fig. 11 AFM topographical images of tested samples. The colour represents the height, and
378 brighter means higher. The solution concentration C was 80 mg/ml, while the samples were
379 spun under different humidity, from 0 to 75% Rh. The z-scale was chosen for the best
380 representation of the coating morphology. A – uniform coatings; B – 20 kDa and 200 kDa
381 blends; C – 91 kDa and 200 kDa blends. (PowerPoint 365, Gwyddion v2.50,
382 <http://gwyddion.net>)

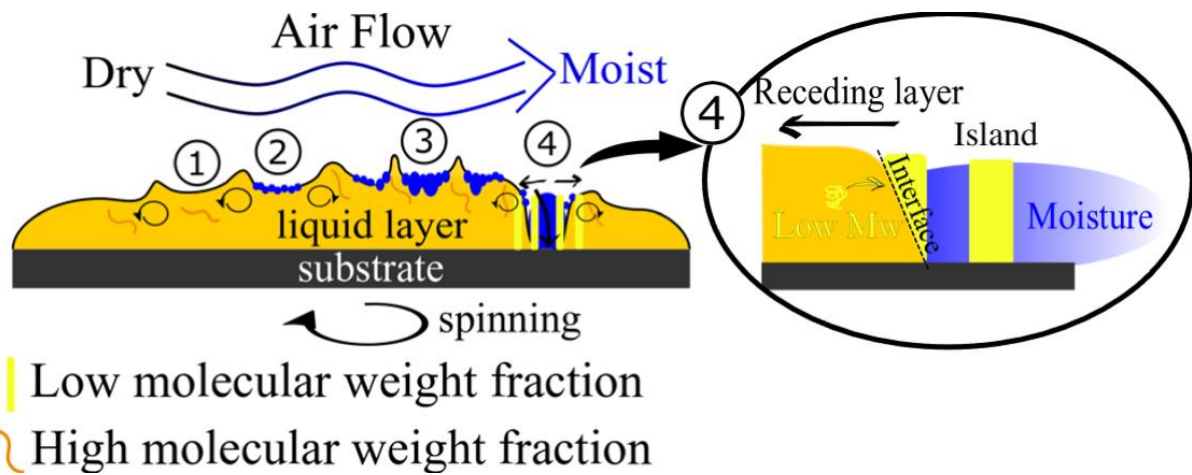
383

384 We observed that smaller cavities (breath figures) formed around the larger cavities caused by
385 dewetting-related polymeric film ruptures. The structure that resembles the honeycomb also
386 occurred. For Rh 55%, a honeycomb-like morphology is found for all coatings, except the
387 uniform 20 kDa coating. It is difficult to distinguish uniform samples from the 90 kDa 200 kDa
388 blend. However, the 20 kDa and 200 kDa blends have distinctive morphology that depends on
389 the PDI value. Radially averaged power spectral density analysis (SI, Fig. S9) of four averaged
390 images depicts the differences between the 75/25, 50/50, and 25/75 w/w% 20 kDa and 200 kDa
391 coatings.

392 Interestingly, the coatings prepared from 20 kDa and 200 kDa bimodal blends at Rh 75% had
393 polymeric islands inside the large holes. The onset of such structures can also be observed in
394 the case of coatings prepared in Rh 55%. The fraction of the islands decreased with an increase
395 in the 200 kDa contribution. It was assumed that the islands are made of a lighter and less
396 viscous fraction. Seemingly, the heavier polymer fraction, more viscous and more entangled,
397 reinforced the honeycomb cell borders. The possible scenario is illustrated in Fig. 12. The
398 coatings at Rh 0%, 45%, 55%, and 75% are marked by numbers 1, 2, 3, and 4, respectively. It
399 is assumed that MEK did not evaporate entirely and formed MEK/20 kDa and MEK/200 kDa
400 fractions. It should be noted that MEK is also soluble in water. Thus, some fraction of the
401 solvent can diffuse to the water phase. The MEK/20 kDa fraction becomes dispersed in the

402 water area of the sample. The MEK/200kDa fraction forms the walls of the cells. Two
 403 explanations can be proposed. First, as shown above, the rheological properties of 200 kDa and
 404 20 kDa polystyrene species differ. The more entangled 200 kDa chains act together, while the
 405 20 kDa chains separate from the high-tension region (higher molecular weight) towards the
 406 water/MEK interface. However, water has very high polarity. Very nonpolar polystyrene forms
 407 a round shape in contact. Furthermore, as was demonstrated, the solvent would deplete the 20
 408 kDa fraction faster than the 200 kDa fraction, allowing for faster solidification of the 20 kDa
 409 islands.

410



412

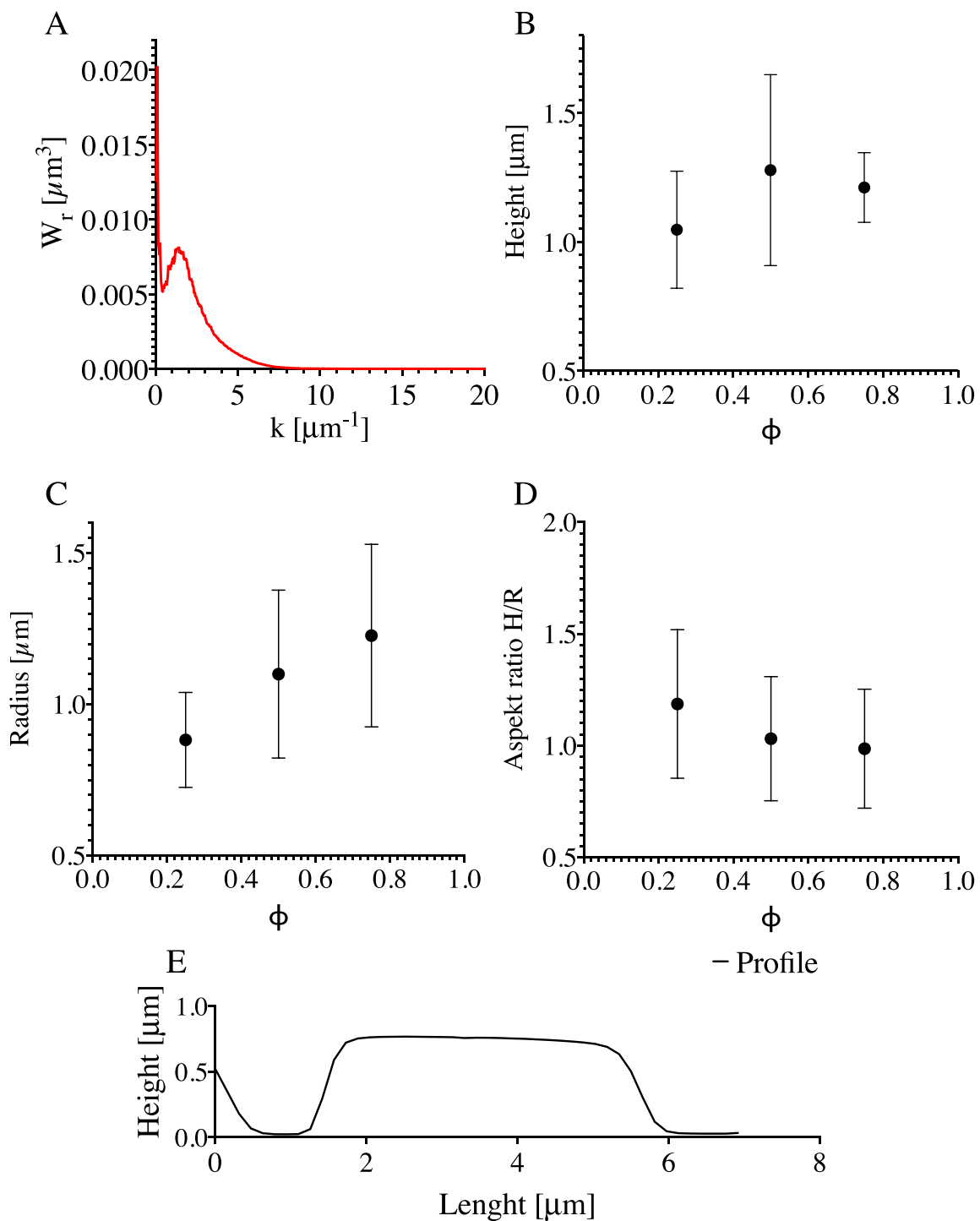
412 Fig. 12. Four scenarios of phase separation: spin-coating in dry air ((1), 0% Rh); moderate
 413 humidity ((2), 45% Rh; (3), 55% Rh); and high humidity ((4), 75% Rh). Low and high
 414 molecular weight fractions, convective flow driving honeycomb formation, and low molecular
 415 weight separation at the interface between the water-wetted rupture and the liquid layer of the
 416 polymer solution are presented. (Inkscape v0.92, <https://inkscape.org/>);

417

418 Second, it can be discussed in terms of the two-step phase separation process discussed by
 419 Henderson et al. Their study focused on modelling the two-step quench scenario. First, the
 420 solution undergoes a temperature quench into the spinodal decomposition region. After a
 421 specific time, a secondary quench was enacted by a further decrease in the temperature. As a

422 result, secondary domains appeared inside the already formed structures.(34) The morphology
423 discussed was very similar to that discussed in the current paper. The presented power spectra
424 of the optical images of the 75/25 w/w% 20 kDa and 200 kDa coatings presented in Fig. 13A
425 coincide with the results presented in the abovementioned paper. Nevertheless, in the current
426 experiment, the first temperature quench is followed by the condensation of water. A decrease
427 in temperature may facilitate the phase separation of polystyrene. Conversely, condensation
428 should coincide with an increase in temperature. (23) However, water may be absorbed by
429 MEK. The MEK/water composition would be a much poorer solvent for PS. Thus, secondary
430 quenching would occur due to the change in solvent quality by water.

431 Fig. 13 presents the characteristic values describing the shape of the islands, Fig. 13 B – height
432 H, Fig. 13 C - radius R, Fig. 13 D - aspect ratio H/R and Fig. 13 E – profile of an island. The
433 dependence of the shape on the fraction of 20 kDa PS can be pointed out.



434

435 Fig. 13. A – Power spectra of islands/honeycomb morphology. B – Mean height, H , of islands

436 with respect to the fraction of 20 kDa PS, ϕ . C – Mean radius of islands, R . D – mean aspect

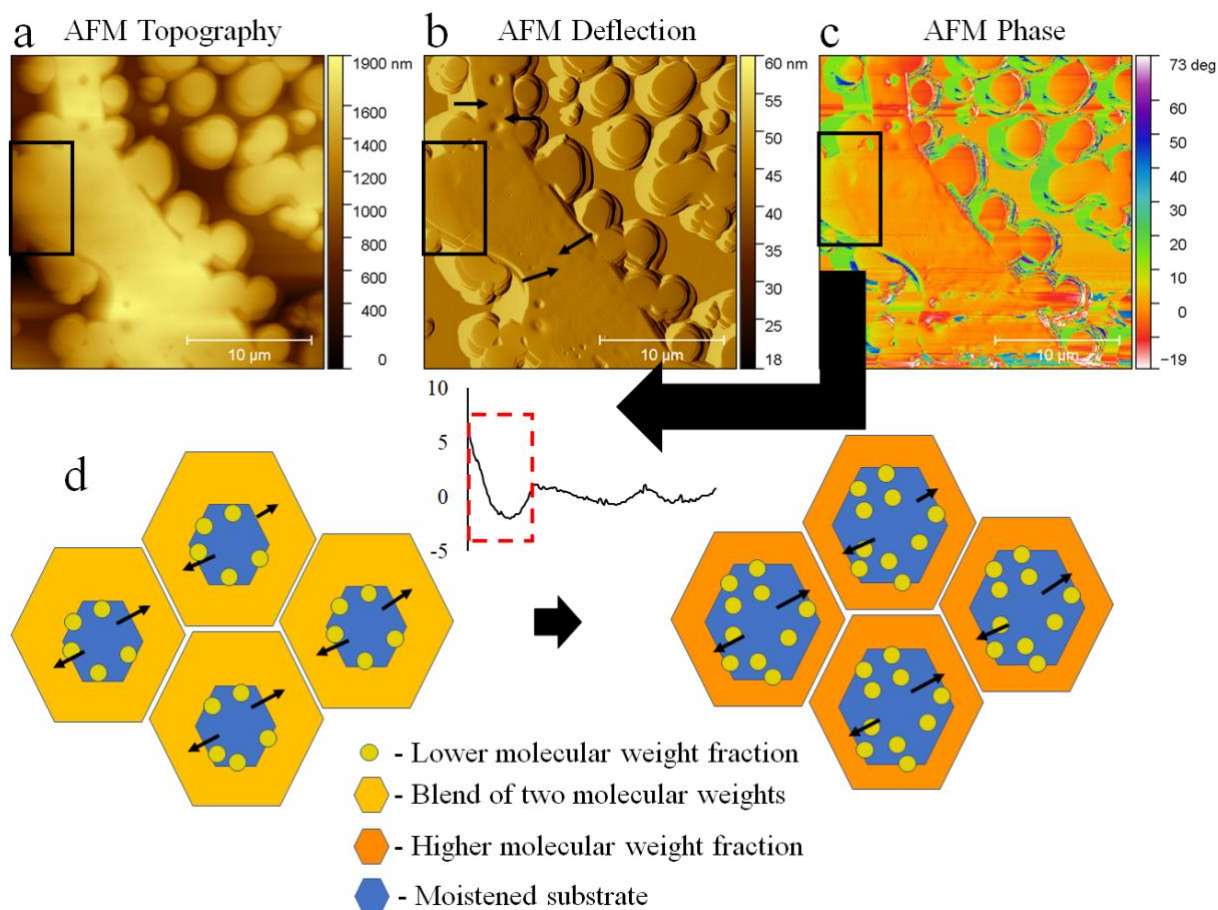
437 ratio of islands, H/R . H profile of an island. (GraphPad Prism 9, <https://www.graphpad.com>)

438

439 Additionally, we tested the formation of micro islands when a short spin-coating time was used
440 (0.5 s and 1 s). These images are presented in Fig. S15 in SI. Secondary phase separation has
441 already been seen, although the islands were not fully formed.

442 The AFM image (Fig. 14 a-c) shows the event of the low molecular weight fraction separating
443 from the cell border. Cracks between the two phases and the spot where the partially formed
444 island disconnects from the bulk can be seen. The black rectangle indicates the area that differed
445 in terms of the deflection signal and phase contrast. However, the discussed phenomenon
446 appears after the thin film of the solution was formed on the substrate. The condensation
447 required time to make holes in the films. The dewetting of the substrate by the solution can
448 induce additional motion of molecules, allowing the lower molecular weight fraction to
449 precipitate. Water would also change the surface tension locally and induce the thermocapillary
450 effects that lead to the formation of convection cells (depicted in Fig 14 d).

451



452

453 Fig. 14. AFM magnification of the cell border of the 20 kDa and 200 kDa 75/25 w/w% blend

454 spun at Rh 75%. The black rectangle indicates the separation of different phases. The same

455 region is shown in the form of a - topography, b - AFM deflection, the direction of dewetting

456 is indicated by the black arrows; c - AFM phase image, an arrow indicates the phase signal

457 difference presented as the averaged cross-section of the marked region (black box); d –

458 schematic illustration depicting proposed formation mechanism of the honeycomb; Convection

459 inside the liquid film led to cells formation, condensation of water led to film rupture (Blue).

460 Subsequently, the recess of the film occurred. At the interface between the rupture area and the

461 receding film, separation of the lower molecular fraction arises (yellow). Subsequently, the cell

462 borders were reinforced by the remaining high molecular weight fraction (Orange);

463 (PowerPoint 367; Inkscape v0.92, <https://inkscape.org>; Gwyddion v2.50, <http://gwyddion.net>)

464

465 As mentioned, the polystyrenes used were unmodified standard grade polymers. The unchanged
466 chemical composition of the coatings was confirmed by FTIR spectroscopy (SI Fig. S10 – S12).
467 The recognized functional groups were CH₃, CH₂, and phenyl groups. These groups are
468 hydrophobic and were the driving force behind the dewetting process under high humidity
469 conditions. This argument was further reinforced by the free surface energy (SEF) measurement
470 (SI Figs. S13 – S14). The SEF of the 20 kDa coating was slightly higher than that of the 200
471 kDa coating and, consequently, led to a higher affinity for the hydrophilic SiO₂ substrate of the
472 former coating.

473

474 **Conclusions**

475 To the best of our knowledge, we have demonstrated for the first time phase separation in a
476 solution of polystyrenes with identical chemical structures but different molecular weights.
477 Phase separation was found for 90 kDa and 200 kDa blends and 20 kDa and 200 kDa blends.
478 In both cases, phase separation was found for 75/25 and 50/50 w/w%. Force spectroscopy was
479 used to determine the different phases in the coatings. Phase separation was discussed in terms
480 of the difference in the viscosity of polystyrene species. Next, we provoked secondary phase
481 separation by introducing water vapor. We have theorized that water vapor would act two-fold.
482 The water droplets formed breath figures, and as the vapor concentration increased, they caused
483 ruptures in the liquid film. Second, the absorption of vapor by methyl ethyl ketone, a solvent
484 chosen due to its hygroscopic properties, would decrease the solubility of polystyrene. We
485 observed secondary phase separation for the 20 kDa and 200 kDa blends. But not for 90 kDa
486 and 200 kDa blends. We also pointed out that the internal thermocapillary convection and
487 gradient of the surface tension of the top layer formed convection cells inside the liquid. The
488 ruptures caused by condensation, with the combination of convection and thermocapillary

489 effects, formed honeycombs. The secondary phase separation left the dispersed 20 kDa
490 polystyrene phase inside the 200 kDa polystyrene honeycomb.

491 The described mechanism can likely be applied to other solvent-polymer systems, consisting
492 even of three polymer fractions. It is likely possible to apply the described process to other
493 coating methods, such as dip coating, blade coating or ink-jet printing.

494

495 **Experimental**

496 • **Materials**

497 All polymers and solvents were purchased from Sigma Aldrich (Merck KGaA). A one-side
498 polished ultrasmooth SiO_x wafer was purchased from Technolutions Sp. z o. o.

499

500 • **Preparation of the coatings**

501 Analytical standard grade polystyrenes (PS) obtained from the supplier with PDI = 1.04 and
502 $M_w = 20$ kDa, 91 kDa, 150 kDa, or 200 kDa were used.

503 Two kinds of blends were prepared: blends of 20 kDa and 200 kDa PS mixed in 75/25, 50/50,
504 25/75 w/w % proportions; similarly, blends of 91 kDa and 200 kDa PS were mixed in the same
505 proportions and dissolved in methyl ethyl ketone (analytic grade, MEK) and mixed for an hour
506 at 37 °C. After mixing, the solutions were stored overnight. The list of polystyrene blends used
507 is summarized in Table 1. The concentrations of these solutions ranged from 2.5 mg/ml to 80
508 mg/ml. A DIY Arduino-based spin-coater with a chamber with controlled humidity was used
509 to spin polystyrene films onto the SiO_x wafers. The experimental setup is depicted in
510 Supplementary Information (SI) Figs. S1 – S2. A 35 µl aliquot of the solution was pipetted onto
511 a 1 cm x 1 cm wafer. Spin-coating was performed in a closed chamber with a constant airflow
512 of 10 ml/min to maintain the desired humidity. The rotational speed was 2700 rpm or 3300 rpm.

513 The spinning time was set to 10 s to allow the solvent to evaporate. Solutions were spin-coated
 514 under humidity of Rh 0%, 45%, 55%, 75%.

515
 516 Table 1. List of polymer blends that were used for spin-coating.

Type of Blend	Sample code	Molecular weight M_w [kDa]		PDI
Uniform	20 kDa	20		1.04
	91 kDa	91		1.04
	150 kDa	150		1.04
	200 kDa	200		1.04
Bimodal	Sample code	Molecular weight		PDI
		$[M_w]$ [kDa] ₍₁₎	$[M_n]$ [kDa] ⁽²⁾	
91 kDa / 200 kDa	75/25*	137	118	1.16
	50/50*	166	146	1.14
	25/75*	186	173	1.08
20 kDa / 200 kDa	75/25**	158	65	2.43
	50/50**	184	110	1.67
	25/75**	194	155	1.25

517 ⁽¹⁾Weight average molecular weight $[M_w] = (f_1M_{w1}^2 + f_2M_{w2}^2)/(f_1M_{w1} + f_2M_{w2})$, ⁽²⁾Number average molecular
 518 weight $[M_n] = f_1M_{w1} + f_2M_{w2}$, where f - fraction of one of the polymers in %; PDI states for the polydispersity
 519 index.

520

521 • **Gel permeation chromatography (GPC)**

522 The number and weight average molecular weights (M_n and M_w) were determined by an Agilent
 523 1200 series GPC modular system with a refractive index detector (RID) equipped with two
 524 PLgel 5 μ m MIXED-C columns (300x7.5 mm) in the series, while the polydispersity index was
 525 calculated as the ratio of M_w/M_n . Calibration was performed using a set of 12 narrowly
 526 distributed polystyrene standards with molecular weights (M_p s) in the range of 474 g/mol - 1
 527 800 000 g/mol.

528 The measurements were performed at 35 °C. Chloroform GPC grade was used as a solvent at
 529 a flow rate of 0.7 ml/min. All samples (~2 mg/ml) were filtered through a PTFE 0.2 μ m

530 membrane before the analysis. The data were collected by ChemStation for LC and analysed
531 by ChemStation GPC Data Analysis Software.

532

533 • **Force Spectroscopy FS and Elastic Modulus**

534 When a force spectroscopy experiment is performed, an AFM probe applies strain on the film
535 surface.(67) Force spectroscopy was performed by means of atomic force microscopy (AFM,
536 Asylum Research MFP3D Bio). (68) An OMLCT-AC200TS-R3 (Olympus) cantilever was
537 used with the nominal spring constant $k = 9 \text{ N/m}$ and tip radius below 10 nm, as suggested by
538 the cantilever's producer. AFM was calibrated using the built-in thermal vibrations method.
539 The (69) Johnson, Kendall, and Roberts (JKR) model was used to calculate the elastic modulus
540 (E).(70) The indentation depth was $\sim 8 \text{ nm}$ (Supplementary Information, 4. *Force*
541 *Spectroscopy*). As we wanted to neglect the possible influence of stiff (silica) substrate on the
542 polystyrene coating's registered mechanical data, we decided to perform an FS experiment
543 using the thickest films (films spun from the solution of a concentration of 80 mg/ml).
544 Maps of a large area of the coating $80 \mu\text{m} \times 80 \mu\text{m}$ with 40×40 points were obtained. These
545 higher resolution maps are supplemented as an attachment (SI). These data were supported by
546 lower resolution maps with a resolution of 15×15 points. Each map was used to obtain the
547 mean elastic modulus value. Altogether, at least five maps were made. Ordinary one-way
548 ANOVA followed by multiple comparisons Fisher's test was used to compare different groups'
549 means.

550 Furthermore, histograms representing each higher resolution map were prepared. The skewness
551 of the elastic modulus distribution was measured. Skewness was divided into two groups: one
552 for uniform coatings and one for bimodal coatings. The t-test ($p < 0.05$) was used to compare
553 the means of these two groups.

554

555 • **Evaluation of the thickness of spin-coated films by means of atomic force**
556 **microscopy**

557 The thickness of spin-coated films was assessed based on intentionally made scratch
558 topography images (SI Fig. S3). Five randomly selected areas of each sample were tested, and
559 profiles were generated. Each of the profile lines was averaged from three contiguous lines to
560 avoid any unwanted artefacts.

561

562 • **Imaging of the coatings**

563 Inverted light microscopes (Nikon EPIPHOT 200 and Zeiss Axio Observer) were used for
564 imaging. An atomic force microscope (AFM, Asylum Research MFP3D Bio) working in
565 tapping mode (AC mode) was used to illustrate the phase composition and topography of the
566 polystyrene films.

567

568 • **In situ measurement of evaporation during spin-coating through laser light**
569 **reflectometry with stroboscopic effect**

570 In situ stroboscopic laser light reflectometry was developed to investigate the thinning of the
571 solution layer while spinning. The laser light is reflected from the coating during the spin-
572 coating process. The occurring interference pattern can be used to estimate the thinning rate of
573 the solution. (71–73) The experimental setup is described in SI, Figs. S1 – S2.

574 Depending on the thickness of the layer, constructive or destructive interference can occur. The
575 condition for the constructive interference was calculated from Bragg's law: $2n\Delta h\cos\theta = m\lambda$,
576 where n is the refractive index of the layer, Δh is the thickness of the layer, θ is the incident
577 angle, m is an integer number, and λ is the light wavelength. For pure MEK, $\Delta h = 235$ nm
578 (assuming the refractive index MEK = 1.3788). For the polymer solution, it was assumed that

579 the refractive index was $n = 1.5$; thus, $\Delta h = 217$ nm. The laser light wavelength was $\lambda = 650$
580 nm. The time resolution was 0.022 s.

581

582 • **Data analysis and visualisation**

583 For data visualization and analysis: Microsoft PowerPoint 365, Inkscape v0.92, and GraphPad
584 Prism was used. Image analysis procedures implemented in Gwyddion software (ver 2.50) and
585 Igor Pro 6.37 with Asylum Research 15.02.105 add-on were used. Spectragryph v1.5.15 was
586 used for FTIR analysis.

587

588 • **Fourier Transform IR**

589 Infrared spectra were collected using a Fourier transform infrared spectrophotometer (Nicolet
590 8700 FTIR, Thermo Scientific). Measurements were performed using FTIR ATR over a range
591 of 4000–400 cm^{-1} .

592

593 • **Contact Angle and Surface Free Energy Measurement**

594 The contact angle (CA) was measured using a Data Physics OCA 20 goniometer. The contact
595 angle was measured with a sessile drop method. For surface free energy measurement (SFE),
596 two kinds of coatings were chosen: 20 kDa and 200 kDa. For each type of coating, three droplets
597 were measured, and three different coatings were used. Two liquid systems were used:
598 deionised water and diiodomethane (Sigma Aldrich, Analytic grade). The groups were
599 compared with the t-test ($p < 0.05$). The Owens, Wendt, Rabel, and Kaelble (OWKR) method
600 was used for SFE calculation. (74)

601

602 **Supporting Information (SI)**

603 Experimental setup depicting the custom-built spin-coater with a humidity-controlled chamber
604 and an in situ interferometer with the stroboscopic effect. Illustration of thickness measurement.
605 Viscosity-related coefficients. Optical microscope images. FTIR results. Free Surface Energy
606 results.

607

608 **Author information**

609 Corresponding authors:

610 Maciej Łojkowski, ORCID: 0000-0002-0612-7964, email: 00183042@pw.edu.pl

611 Wojciech Swieszkowski, ORCID: 0000-0003-4216-9974, email:

612 wojciech.swieszkowski@pw.edu.pl.

613

614 The authors declare no competing financial interest.

615

616 **Acknowledgements**

617 This manuscript is a part of Maciej Łojkowski PhD thesis. This work was supported by
618 the National Centre for Research and Developments
619 [STRATEGMED3/306888/3/NCBR/2017]. We are grateful Mgr. Donata Kuczyńska-Zemła
620 for help with optical microscopy.

621

622 **Authors contributions:**

623 Conceptualization, M.Ł. ; methodology, M.Ł., A.Ch., E.Ch. ; investigation, M.Ł., A.Ch., E.
624 Ch., imaging, M.Ł., A.Ch. ; data analysis, M.Ł. ; visualisation, M.Ł. ; writing, M.Ł. ;
625 supervision, W. Ś.; revision of the manuscript, M.Ł., A.Ch., E. Ch., W. Ś; funding acquisition
626 W. Ś. All authors have read and agreed to the published version of the manuscript.

627

628 **Abbreviations**

629 AFM – atomic force microscopy; bimodal – polymer with two nodes in molecular weight
630 distribution; coating – final polymer coating; CA – contact angle; E – elastic modulus; film –
631 liquid film of solution spread on the substrate; FS – force spectroscopy; FTIR – Fourier
632 transform IR; GPC – gel permeation chromatography; initial solution – solution at the start of
633 spin-coating; MEK – methyl ethyl ketone; Mw – molecular weight; $[M_w]$ – weight average
634 molecular weight; $[M_n]$ – number average molecular weight; MWD – molecular weight
635 distribution; PDI – polydispersity index; PTF – polymer thin film; PS – polystyrene; Rh% -
636 relative humidity in %; RMS – root mean square roughness; uniform – polymer with one node
637 in molecular weight distribution.

638

639 **References**

- 640 1. Kumar M, Bhardwaj R. Wetting characteristics of *Colocasia esculenta* (Taro) leaf and a
641 bioinspired surface thereof. *Sci Rep.* 2020;10(1):1–15.
- 642 2. He R, Xiao J, Zhang M, Zhang Z, Zhang W, Cao Y, et al. Artificial honeycomb-
643 inspired TiO₂ nanorod arrays with tunable nano/micro interfaces for improving
644 poly(dimethylsiloxane) surface hydrophobicity. *J Mater Sci.* 2016;51(6):2935–41.
- 645 3. Jahed Z, Shahsavan H, Verma MS, Rogowski JL, Seo BB, Zhao B, et al. Bacterial
646 Networks on Hydrophobic Micropillars. *ACS Nano.* 2017;11(1):675–83.
- 647 4. Liu X, Liu R, Cao B, Ye K, Li S, Gu Y, et al. Subcellular cell geometry on micropillars
648 regulates stem cell differentiation. *Biomaterials* [Internet]. 2016 Dec;111:27–39.
649 Available from: <http://dx.doi.org/10.1016/j.biomaterials.2016.09.023>
- 650 5. Walheim S, Böltau M, Mlynek J, Krausch G, Steiner U. Structure Formation via
651 Polymer Demixing in Spin-Cast Films. *Macromolecules* [Internet]. 1997 Aug
652 1;30(17):4995–5003. Available from: <https://doi.org/10.1021/ma9619288>

- 653 6. Daly R, Sader JE, Boland JJ. The dominant role of the solvent–water interface in water
654 droplet templating of polymers. *Soft Matter* [Internet]. 2013;9(33):7960. Available
655 from: <http://xlink.rsc.org/?DOI=c3sm51452h>
- 656 7. Khikhlovskiy V, Wang R, van Breemen AJJM, Gelinck GH, Janssen RAJ, Kemerink
657 M. Nanoscale Organic Ferroelectric Resistive Switches. *J Phys Chem C* [Internet].
658 2014 Feb 13;118(6):3305–12. Available from:
659 <https://pubs.acs.org/doi/10.1021/jp409757m>
- 660 8. D’Andrade BW, Forrest SR. White Organic Light-Emitting Devices for Solid-State
661 Lighting. *Adv Mater* [Internet]. 2004 Sep 16;16(18):1585–95. Available from:
662 <http://doi.wiley.com/10.1002/adma.200400684>
- 663 9. Yabu H. Fabrication of honeycomb films by the breath figure technique and their
664 applications. *Sci Technol Adv Mater* [Internet]. 2018;19(1):802–22. Available from:
665 <https://doi.org/10.1080/14686996.2018.1528478>
- 666 10. Wu D, Xu F, Sun B, Fu R, He H, Matyjaszewski K. Design and Preparation of Porous
667 Polymers. *Chem Rev* [Internet]. 2012 Jul 11;112(7):3959–4015. Available from:
668 <https://pubs.acs.org/doi/10.1021/cr200440z>
- 669 11. Karagkiozaki V, Vavoulidis E, Karagiannidis PG, Gioti M, Fatouros DG, Vizirianakis
670 IS, et al. Development of a nanoporous and multilayer drug-delivery platform for
671 medical implants. *Int J Nanomedicine*. 2012;7(October):5327–38.
- 672 12. Calejo MT, Ilmarinen T, Skottman H, Kellomäki M. Breath figures in tissue
673 engineering and drug delivery: State-of-the-art and future perspectives. Vol. 66, *Acta*
674 *Biomaterialia*. 2018.
- 675 13. Vendra VK, Wu L, Krishnan S. Polymer Thin Films for Biomedical Applications. In:
676 *Nanotechnologies for the Life Sciences* [Internet]. Weinheim, Germany: Wiley-VCH
677 Verlag GmbH & Co. KGaA; 2011. Available from:

- 678 <http://doi.wiley.com/10.1002/9783527610419.ntls0179>
- 679 14. Griesser HJ. *Thin Film Coatings for Biomaterials and Biomedical Applications*, 1st
680 Edition. 2016. 310 p.
- 681 15. Łojkowski M, Walheim S, Jokubauskas P, Schimmel T, Świążkowski W. Tuning the
682 wettability of a thin polymer film by gradually changing the geometry of nanoscale
683 pore edges. *Langmuir* [Internet]. 2019;35(17):5987–96. Available from:
684 <https://doi.org/10.1021/acs.langmuir.9b00467>
- 685 16. Plawsky JL, Kim JK, Schubert EF. Engineered nanoporous and nanostructured films.
686 *Mater Today* [Internet]. 2009;12(6):36–45. Available from:
687 [http://dx.doi.org/10.1016/S1369-7021\(09\)70179-8](http://dx.doi.org/10.1016/S1369-7021(09)70179-8)
- 688 17. Bormashenko E. Breath-figure self-assembly, a versatile method of manufacturing
689 membranes and porous structures: Physical, chemical and technological aspects.
690 *Membranes* (Basel). 2017;7(3).
- 691 18. Birnie DP. Rational solvent selection strategies to combat striation formation during
692 spin coating of thin films. *J Mater Res*. 2001;16(4):1145–54.
- 693 19. van Franeker JJ, Westhoff D, Turbiez M, Wienk MM, Schmidt V, Janssen RAJ.
694 Controlling the Dominant Length Scale of Liquid-Liquid Phase Separation in Spin-
695 coated Organic Semiconductor Films. *Adv Funct Mater* [Internet]. 2015
696 Feb;25(6):855–63. Available from: <http://doi.wiley.com/10.1002/adfm.201403392>
- 697 20. Schaefer C, Michels JJ, van der Schoot P. Structuring of Thin-Film Polymer Mixtures
698 upon Solvent Evaporation. *Macromolecules* [Internet]. 2016 Sep 27;49(18):6858–70.
699 Available from: <https://pubs.acs.org/doi/10.1021/acs.macromol.6b00537>
- 700 21. Ebbens S, Hodgkinson R, Parnell AJ, Dunbar A, Martin SJ, Topham PD, et al. In Situ
701 Imaging and Height Reconstruction of Phase Separation Processes in Polymer Blends
702 during Spin Coating. *ACS Nano* [Internet]. 2011 Jun 28;5(6):5124–31. Available from:

- 703 <https://pubs.acs.org/doi/10.1021/mn201210e>
- 704 22. Danglad-Flores J, Eickelmann S, Riegler H. Deposition of polymer films by spin
705 casting: A quantitative analysis. *Chem Eng Sci* [Internet]. 2018 Apr;179:257–64.
706 Available from: <https://linkinghub.elsevier.com/retrieve/pii/S0009250918300125>
- 707 23. Dombrovsky LA, Frenkel M, Legchenkova I, Bormashenko E. Effect of thermal
708 properties of a substrate on formation of self-arranged surface structures on evaporated
709 polymer films. *Int J Heat Mass Transf* [Internet]. 2020;158:120053. Available from:
710 <https://doi.org/10.1016/j.ijheatmasstransfer.2020.120053>
- 711 24. Daly R, Sader JE, Boland JJ. Taming Self-Organization Dynamics to Dramatically
712 Control Porous Architectures. *ACS Nano* [Internet]. 2016 Mar 22;10(3):3087–92.
713 Available from: <https://pubs.acs.org/doi/10.1021/acsnano.5b06082>
- 714 25. Zabusky HH, Heitmiller RF. Properties of high density polyethylenes with bimodal
715 molecular weight distribution. *Polym Eng Sci*. 1964;4(1):17–21.
- 716 26. Wu BH, Zhong QZ, Xu ZK, Wan LS. Effects of molecular weight distribution on the
717 self-assembly of end-functionalized polystyrenes. *Polym Chem*. 2017;8(29):4290–8.
- 718 27. Jiang H, Zhang L, Qin J, Zhang W, Cheng Z, Zhu X. Producing bimodal molecular
719 weight distribution polymers through facile one-pot/one-step RAFT polymerization. *J*
720 *Polym Sci Part A Polym Chem*. 2012;50(19):4103–9.
- 721 28. Whitfield R, Parkatzidis K, Truong NP, Junkers T, Anastasaki A. Tailoring Polymer
722 Dispersity by RAFT Polymerization: A Versatile Approach. *Chem* [Internet]. 2020
723 Jun;6(6):1340–52. Available from:
724 <https://linkinghub.elsevier.com/retrieve/pii/S2451929420301923>
- 725 29. Tanaka K, Takahara A, Kajiyama T. Effect of Polydispersity on Surface Molecular
726 Motion of Polystyrene Films. *Macromolecules* [Internet]. 1997 Oct;30(21):6626–32.
727 Available from: <https://pubs.acs.org/doi/10.1021/ma970057e>

- 728 30. Heitmiller RF, Naar RZ, Zabusky HH. Effect of homogeneity on viscosity in capillary
729 extrusion of polyethylene. *J Appl Polym Sci* [Internet]. 1964 Mar;8(2):873–80.
730 Available from: <http://doi.wiley.com/10.1002/app.1964.070080226>
- 731 31. Koningsveld R, Chermin HAG, Gordon M. Liquid–liquid phase separation in
732 multicomponent polymer solutions - VIII. Stability limits and consolute states in quasi-
733 ternary mixtures. *Proc R Soc London A Math Phys Sci* [Internet]. 1970 Oct
734 27;319(1538):331–49. Available from:
735 <https://royalsocietypublishing.org/doi/10.1098/rspa.1970.0182>
- 736 32. Zeman L, Patterson D. Effect of the Solvent on Polymer Incompatibility in Solution.
737 *Macromolecules* [Internet]. 1972 Jul;5(4):513–6. Available from:
738 <https://pubs.acs.org/doi/abs/10.1021/ma60028a030>
- 739 33. Shultz AR, Flory PJ. Phase Equilibria in Polymer—Solvent Systems 1,2. *J Am Chem*
740 *Soc* [Internet]. 1952 Oct 1;74(19):4760–7. Available from:
741 <https://doi.org/10.1021/ja01139a010>
- 742 34. Henderson IC, Clarke N. Two-Step Phase Separation in Polymer Blends.
743 *Macromolecules*. 2004;37(5):1952–9.
- 744 35. Tanaka H. Viscoelastic phase separation in soft matter and foods. *Faraday Discuss*.
745 2012;158:371–406.
- 746 36. Hengeller L, Huang Q, Dorokhin A, Alvarez NJ, Almdal K, Hassager O. Stress
747 relaxation of bi-disperse polystyrene melts: Exploring the interactions between long
748 and short chains in non-linear rheology. *Rheol Acta*. 2016;55(4):303–14.
- 749 37. Harris EK. Effect of blending on the rheological properties of polystyrene. *J Appl*
750 *Polym Sci* [Internet]. 1973 Jun;17(6):1679–92. Available from:
751 <http://doi.wiley.com/10.1002/app.1973.070170604>
- 752 38. Klein J. The Onset of Entangled Behavior in Semidilute and Concentrated Polymer

- 753 Solutions. *Macromolecules* [Internet]. 1978 Sep;11(5):852–8. Available from:
754 <https://pubs.acs.org/doi/abs/10.1021/ma60065a002>
- 755 39. Hong KM, Noolandi J. Theory of inhomogeneous multicomponent polymer systems.
756 *Macromolecules* [Internet]. 1981 May;14(3):727–36. Available from:
757 <https://pubs.acs.org/doi/abs/10.1021/ma50004a051>
- 758 40. Hariharan A, Kumar SK, Russell TP. A lattice model for the surface segregation of
759 polymer chains due to molecular weight effects. *Macromolecules* [Internet]. 1990
760 Jul;23(15):3584–92. Available from:
761 <https://pubs.acs.org/doi/abs/10.1021/ma00217a009>
- 762 41. Mahmoudi P, Matsen MW. Entropic segregation of short polymers to the surface of a
763 polydisperse melt. *Eur Phys J E* [Internet]. 2017 Oct 6;40(10):85. Available from:
764 <http://link.springer.com/10.1140/epje/i2017-11575-7>
- 765 42. Hill JA, Endres KJ, Mahmoudi P, Matsen MW, Wesdemiotis C, Foster MD. Detection
766 of Surface Enrichment Driven by Molecular Weight Disparity in Virtually
767 Monodisperse Polymers. *ACS Macro Lett* [Internet]. 2018 Apr 17;7(4):487–92.
768 Available from: <https://pubs.acs.org/doi/10.1021/acsmacrolett.7b00993>
- 769 43. Stein GE, Laws TS, Verduzco R. Tailoring the Attraction of Polymers toward Surfaces.
770 *Macromolecules* [Internet]. 2019 Jul 9;52(13):4787–802. Available from:
771 <https://pubs.acs.org/doi/10.1021/acs.macromol.9b00492>
- 772 44. Carlier V, Sclavons M, Jonas AM, Jérôme R, Legras R. Probing Thermoplastic
773 Matrix–Carbon Fiber Interphases. 1. Preferential Segregation of Low Molar Mass
774 Chains to the Interface. *Macromolecules* [Internet]. 2001 May;34(11):3725–9.
775 Available from: <https://pubs.acs.org/doi/10.1021/ma000404b>
- 776 45. Suwa J, Kakiage M, Yamanobe T, Komoto T, Uehara H. Molecular Weight
777 Segregation on Surfaces of Polyethylene Blended Films as Estimated from

- 778 Nanoscratch Tests Using Scanning Probe Microscopy. *Langmuir* [Internet]. 2007
779 May;23(11):5882–5. Available from: <https://pubs.acs.org/doi/10.1021/la070150o>
- 780 46. Karim A, Slawacki TM, Kumar SK, Douglas JF, Satija SK, Han CC, et al. Phase-
781 Separation-Induced Surface Patterns in Thin Polymer Blend Films. *Macromolecules*
782 [Internet]. 1998 Feb;31(3):857–62. Available from:
783 <https://pubs.acs.org/doi/10.1021/ma970687g>
- 784 47. Hoppe H, Heuberger M, Klein J. Self-Similarity and Pattern Selection in the
785 Roughening of Binary Liquid Films. *Phys Rev Lett* [Internet]. 2001 May
786 21;86(21):4863–6. Available from:
787 <https://link.aps.org/doi/10.1103/PhysRevLett.86.4863>
- 788 48. Heier J, Kramer EJ, Revesz P, Battistig G, Bates FS. Spinodal Decomposition in a
789 Subsurface Layer of a Polymer Blend Film. *Macromolecules* [Internet]. 1999
790 Jun;32(11):3758–65. Available from: <https://pubs.acs.org/doi/10.1021/ma981709h>
- 791 49. Jandt KD, Heier J, Bates FS, Kramer EJ. Transient surface roughening of thin films of
792 phase separating polymer mixtures. *Langmuir*. 1996;12(15):3716–20.
- 793 50. Huang C, Förste A, Walheim S, Schimmel T. Polymer blend lithography for metal
794 films: Large-area patterning with over 1 billion holes/inch². *Beilstein J Nanotechnol*.
795 2015;6(1):1205–11.
- 796 51. Flory PJ, Höcker H. Thermodynamics of polystyrene solutions. Part 1.—Polystyrene
797 and methyl ethyl ketone. *Trans Faraday Soc* [Internet]. 1971;67:2258–69. Available
798 from: <http://xlink.rsc.org/?DOI=TF9716702258>
- 799 52. Imre A, Van Hook WA. Liquid-liquid demixing from solutions of polystyrene. 1. A
800 review. 2. Improved correlation with solvent properties. Vol. 25, *Journal of Physical*
801 *and Chemical Reference Data*. 1996. p. 637–61.
- 802 53. Utracki LA, Wilkie CA. Polymer blends handbook. *Polymer Blends Handbook*. 2014.

- 803 1–2378 p.
- 804 54. Ying Q, Chu B. Overlap concentration of macromolecules in solution. *Macromolecules*
805 [Internet]. 1987 Mar;20(2):362–6. Available from:
806 <https://pubs.acs.org/doi/abs/10.1021/ma00168a023>
- 807 55. Kim JK, Taki K, Nagamine S, Ohshima M. Periodic porous stripe patterning in a
808 polymer blend film induced by phase separation during spin-casting. *Langmuir*.
809 2008;24(16):8898–903.
- 810 56. Heier J, Kramer EJ, Groenewold J, Fredrickson GH. Kinetics of individual block
811 copolymer island formation and disappearance near an absorbing boundary.
812 *Macromolecules*. 2000;33(16):6060–7.
- 813 57. Coveney S, Clarke N. Pattern formation in polymer blend thin films: Surface
814 roughening couples to phase separation. *Phys Rev Lett*. 2014;113(21):1–5.
- 815 58. Mecke K. Additivity, Convexity, and Beyond: Applications of Minkowski Functionals
816 in Statistical Physics. *Stat Phys Spat Stat* [Internet]. 2000;111–84. Available from:
817 http://link.springer.com/chapter/10.1007/3-540-45043-2_6
- 818 59. Wolf BA. Improvement of polymer solubility: Influence of shear and of pressure. *Pure*
819 *Appl Chem*. 1997;69(5):929–33.
- 820 60. Du B, Tsui OKC, Zhang Q, He T. Study of Elastic Modulus and Yield Strength of
821 Polymer Thin Films Using Atomic Force Microscopy. *Langmuir* [Internet]. 2001
822 May;17(11):3286–91. Available from: <https://pubs.acs.org/doi/10.1021/la001434a>
- 823 61. Landel RF, Nielsen LE. *Mechanical properties of polymers and composites*. CRC
824 press; 1993.
- 825 62. Torres JM, Stafford CM, Vogt BD. Impact of molecular mass on the elastic modulus of
826 thin polystyrene films. *Polymer (Guildf)* [Internet]. 2010;51(18):4211–7. Available
827 from: <http://dx.doi.org/10.1016/j.polymer.2010.07.003>

- 828 63. Kok CM, Rudin A. Prediction of Flory–Huggins interaction parameters from intrinsic
829 viscosities. *J Appl Polym Sci*. 1982;27(2):353–62.
- 830 64. Lee SH, Lee SB. The Hildebrand solubility parameters, cohesive energy densities and
831 internal energies of 1-alkyl-3-methylimidazolium-based room temperature ionic
832 liquids. *Chem Commun*. 2005;(27):3469–71.
- 833 65. Bormashenko E, Malkin A, Musin A, Bormashenko Y, Whyman G, Litvak N, et al.
834 Mesoscopic patterning in evaporated polymer solutions: Poly(ethylene glycol) and
835 room-temperature-vulcanized polyorganosilanes/-siloxanes promote formation of
836 honeycomb structures. *Macromol Chem Phys*. 2008;209(6):567–76.
- 837 66. Uchiyama H, Matsui T, Kozuka H. Spontaneous Pattern Formation Induced by
838 Bénard–Marangoni Convection for Sol–Gel-Derived Titania Dip-Coating Films: Effect
839 of Co-solvents with a High Surface Tension and Low Volatility. *Langmuir* [Internet].
840 2015 Nov 17;31(45):12497–504. Available from:
841 <https://pubs.acs.org/doi/10.1021/acs.langmuir.5b02929>
- 842 67. Zgłobicka I, Chlanda A, Woźniak M, Łojkowski M, Szoszkiewicz R, Mazurkiewicz-
843 Pawlicka M, et al. Microstructure and nanomechanical properties of single stalks from
844 diatom *Didymosphenia geminata* and their change due to adsorption of selected metal
845 ions. *J Phycol*. 2017;53(4).
- 846 68. Chlanda A, Kijeńska-Gawrońska E, Zdunek J, Swieszkowski W. Internal
847 nanocrystalline structure and stiffness alterations of electrospun polycaprolactone-
848 based mats after six months of in vitro degradation. An atomic force microscopy assay.
849 *J Mech Behav Biomed Mater* [Internet]. 2020 Jan;101(August 2019):103437.
850 Available from: <https://linkinghub.elsevier.com/retrieve/pii/S1751616119305156>
- 851 69. Sader JE, Borgani R, Gibson CT, Haviland DB, Michael J, Kilpatrick JI, et al. A virtual
852 instrument to standardise the calibration of atomic force microscope cantilevers. *Rev*

- 853 Sci Instrum [Internet]. 2016 Sep 1;87(9):093711. Available from:
854 <http://dx.doi.org/10.1063/1.4962866>
- 855 70. Wu KC, You HI. Determination of solid material elastic modulus and surface energy
856 based on JKR contact model. *Appl Surf Sci.* 2007;253(20):8530–7.
- 857 71. Toolan DTW. Straightforward technique for in situ imaging of spin-coated thin films .
858 *Opt Eng.* 2015;54(2):024109.
- 859 72. Toolan DTW, Howse JR. Development of in situ studies of spin coated polymer films.
860 *J Mater Chem C.* 2013;1(4):603–16.
- 861 73. Mokarian-Tabari P, Geoghegan M, Howse JR, Heriot SY, Thompson RL, Jones RAL.
862 Quantitative evaluation of evaporation rate during spin-coating of polymer blend films:
863 Control of film structure through defined-atmosphere solvent-casting. *Eur Phys J E.*
864 2010;33(4):283–9.
- 865 74. Drelich JW, Boinovich L, Chibowski E, Volpe C Della, Hołysz L, Marmur A, et al.
866 Contact Angles: History of Over 200 Years of Open Questions. *Surf Innov* [Internet].
867 2019;(March):1–25. Available from:
868 <https://www.icevirtuallibrary.com/doi/10.1680/jsuin.19.00007>

869

870 Fig 1. Exemplary GPC experiment results of bimodal and uniform MWD polystyrene; A -
871 narrow uniform MWD, $M_w = 91$ kDa, PDI 1.04; B – bimodal MWD, blend of $M_w = 91$ kDa,
872 PDI = 1.04 and $M_w = 200$ kDa, PDI = 1.04.

873

874 Fig. 2. Reduced viscosity η_r/C of the solutions, A - η_r/C plotted against the solution's
875 concentration. Curves represent fits for eq. 2; B - η_r/C plotted as a function of the number
876 average molecular weight function. Curves represent the Mark-Houwink equation fit (eq. 3),
877 $[M_n] = f_1M_{w1} + f_2M_{w2}$, where f is w/w % ratio of polymers.

878

879 Fig. 3. The relation between the evaporation rate of solution and the reduced viscosity of
880 solution for polymer concentrations: A - 20 mg/ml, B - 40 mg/ml, and C - 80 mg/ml. The curves
881 represent the Padé approximation trend line.

882

883 Fig. 4. A - Thickness of the coatings with respect to the composition and the concentration. The
884 plot presents data for uniform and 91 kDa/200 kDa solutions. B – Thickness of the coating for
885 80 mg/ml concentration in the blend's molecular weight function. * - Blends of 91 kDa and 200
886 kDa polystyrene; ** - blend of 20 kDa and 200 kDa polystyrene; x/x – w/w% ratio of blended
887 homogeneous polystyrenes. The number average molecular weight $[M_n] = f_1M_{w1} + f_2M_{w2}$,
888 where f w/w. % ratio of polymers. C - RMS roughness of the coatings spun from 80 mg/ml
889 concentration.

890

891 Fig. 5. A - Optical images of coatings spun from 80 mg/ml. The B - Minkowski connectivity
892 $C(\nu)$ of the coatings spun from 80 mg/ml, where ν represents the threshold for image
893 binarization. The values on the axis were normalized to 1.

894

895 Fig. 6. Average elastic modulus obtained based on the FS method for coatings made from a
896 solution of 80 mg/ml. Uniform – coatings were made from homogeneous solutions; bimodal –
897 coatings made from solutions with bimodal MWD; * - blends of 91 kDa and 200 kDa
898 polystyrene; ** - blend of 20 kDa and 200 kDa polystyrene; x/x – w/w% ratio of blended
899 homogeneous polystyrenes. $[M_n] = f_1M_{w1} + f_2M_{w2}$, where f w/w % ratio of polymers. *** -
900 means are significantly different (one-way ANOVA, $p < 0.05$).

901

902 Fig. 7. Force spectroscopy maps of bimodal MWD coatings and corresponding histograms of
903 the elastic modulus. The greyscale shows the stiffness – the white colour corresponds to the
904 highest stiffness. The grayscale range is ± 1 GPa.

905

906 Fig. 8. Force spectroscopy maps of coatings with uniform MWD and corresponding histograms
907 of the elastic modulus. The greyscale shows the stiffness – the white colour corresponds to the
908 highest stiffness. The grayscale range is ± 1 GPa.

909

910 Fig 9. The skewness of the elastic modulus data sets. Uniform – grouped means that represents
911 the skewness of histograms of uniform coatings elastic modulus. Bimodal – grouped means that
912 represents the skewness of histograms of all kinds of bimodal blends elastic modulus. The
913 means of these two groups were significantly different ($p < 0.05$).

914

915 Fig. 10. The effective miscibility parameter δ_{eff} of the polystyrenes in MEK with bimodal and
916 uniform distributions for two kinds of bimodal distributions: 20 kDa/200 kDa – brown squares
917 and 91 kDa/200 kDa – purple triangles; the blue circles represent data for polystyrenes with
918 uniform distributions. $[M_n] = f_1M_{w1} + f_2M_{w2}$, where f w/w % ratio of polymers.

919

920 Fig. 11 AFM topographical images of tested samples. The colour represents the height, and
921 brighter means higher. The solution concentration C was 80 mg/ml, while the samples were
922 spun under different humidity, from 0 to 75% Rh. The z-scale was chosen for the best
923 representation of the coating morphology. A – uniform coatings; B – 20 kDa and 200 kDa
924 blends; C – 91 kDa and 200 kDa blends.

925

926 Fig. 12. Four scenarios of phase segregation: spin-coating in dry air ((1), 0% Rh); moderate
927 humidity ((2), 45% Rh; (3), 55% Rh); and high humidity ((4), 75% Rh). Low and high
928 molecular weight fractions, convective flow driving honeycomb formation, and low molecular
929 weight separation at the interface between the water-wetted rupture and the liquid layer of the
930 polymer solution are presented.

931

932 Fig. 13. A – Power spectra of islands/honeycomb morphology. B – Mean height, H , of islands
933 with respect to the fraction of 20 kDa PS, ϕ . C – Mean radius of islands, R . D – mean aspect
934 ratio of islands, H/R . H profile of an island.

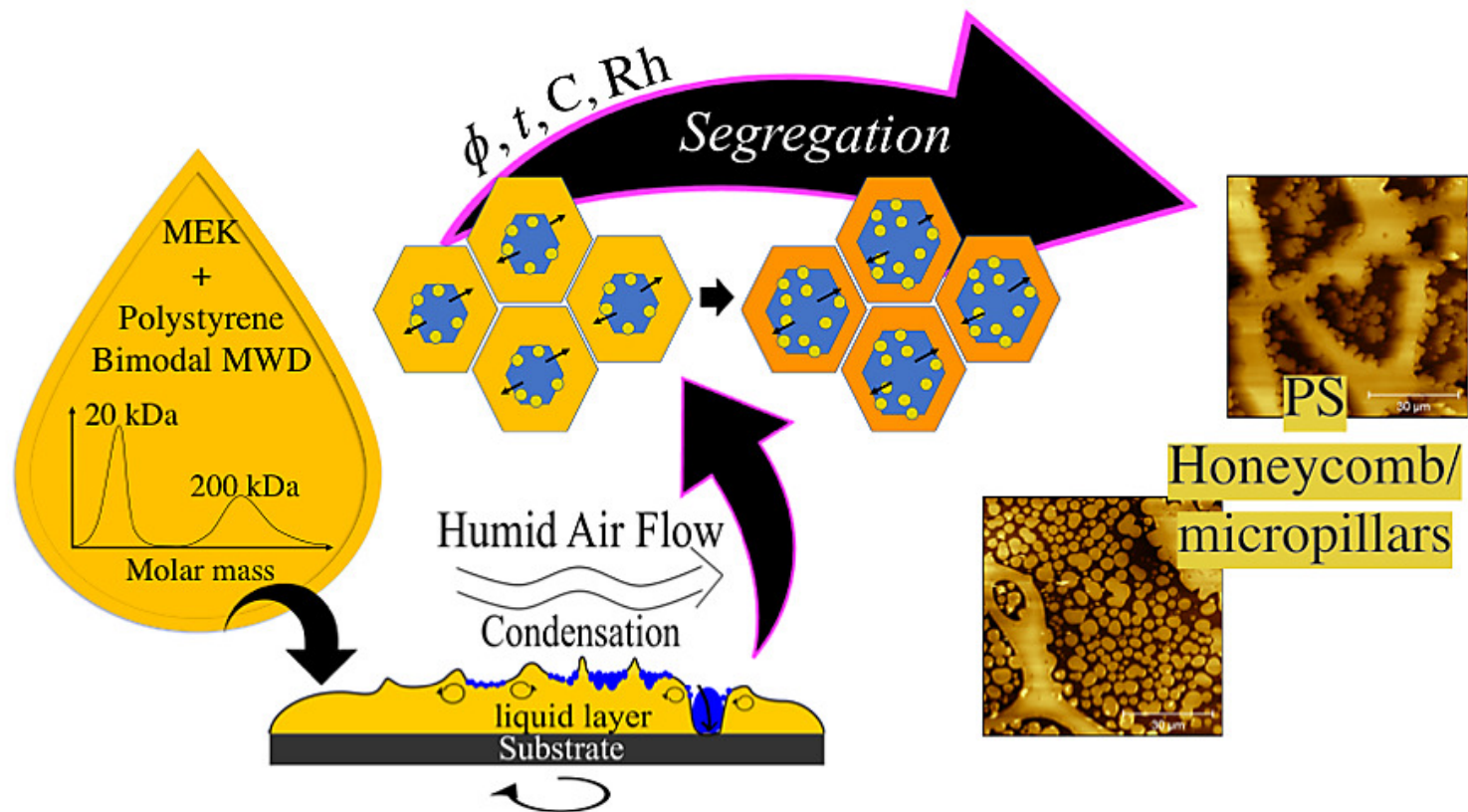
935

936 Fig. 14. AFM magnification of the cell border of the 20 kDa and 200 kDa 75/25 w/w% blend
937 spun at Rh 75%. The black rectangle indicates the separation of different phases. The same
938 region is shown in the form of a - topography, b - AFM deflection, the direction of dewetting
939 is indicated by the black arrows; c - AFM phase image, an arrow indicates the phase signal
940 difference presented as the averaged cross-section of the marked region (black box); d –
941 schematic illustration depicting proposed formation mechanism of the honeycomb; Convection
942 inside the liquid film led to cells formation, condensation of water led to film rupture (Blue).
943 Subsequently, the recess of the film occurred. At the interface between the rupture area and the
944 receding film, segregation of the lower molecular fraction arises (yellow). Subsequently, the
945 cell borders were reinforced by the remaining high molecular weight fraction (Orange);

946

Masło w masle_May21.pdf (1.98 MiB)

[view on ChemRxiv](#) • [download file](#)



TOC.tiff (1.65 MiB)

[view on ChemRxiv](#) • [download file](#)

Supporting information.

Water vapor induced self-assembly of islands/honeycomb structure by secondary phase separation in polystyrene solution with bimodal molecular weight distribution

Authors: Maciej Łojkowski^{1,*}, Adrian Chlanda^{1,2}, Emilia Choińska¹, Wojciech Swieszkowski^{1*}.

Affiliation:

1. Faculty of Material Sciences and Engineering, Warsaw University of Technology, Wołoska 141, 02-507 Warsaw, Poland
2. Department of Chemical Synthesis and Flake Graphene, Institute of Electronic Materials Technology, Wólczyńska 133, 01-919 Warsaw, Poland

*Corresponding authors:

Maciej Łojkowski*, ORCID: 0000-0002-0612-7964, email: 00183042@pw.edu.pl

Wojciech Swieszkowski*, ORCID: 0000-0003-4216-9974, email:

wojciech.swieszkowski@pw.edu.pl.

Number of Pages	31
Number of Figures	15
Number of Tables	16

Table of content

1. Experimental setup description

Fig. S1. DIY spin-coater with humidity controller and laser reflectometer.

Fig. S2. Evaporation rate by laser reflectometry.

2. Film thickness analysis.

Fig. S3 Illustration of thickness measurement

3. Viscosity analysis

Table S1. K and $[\eta]$ coefficients, 95% confidence interval CI; goodness of the fit.

Table S2. Coefficients for Mark-Houwink equation.

Table S3. Dynamic viscosity values of the uniform solutions in cP.

4. Force Spectroscopy analysis

Table S4. Blend of 20 kDa and 200 kDa polystyrene; 75/25 w/w%; Rh 0%.

Table S5. Blend of 20 kDa and 200 kDa polystyrene; 50/50 w/w%; Rh 0%.

Table S6. Blend of 20 kDa and 200 kDa polystyrene; 25/75 w/w%; Rh 0%.

Table S7. Blend of 91 kDa and 200 kDa polystyrene; 75/25 w/w%; Rh 0%.

Table S8. Blend of 91 kDa and 200 kDa polystyrene; 50/50 w/w%; Rh 0%.

Table S9. Blend of 91 kDa and 200 kDa polystyrene; 25/75 w/w%; Rh 0%.

Table S10. 20 kDa uniform polystyrene standard; Rh 0%.

Table S11. 91 kDa uniform polystyrene standard; Rh 0%.

Table S12. 150 kDa uniform polystyrene standard; Rh 0%.

Table S13. 200 kDa uniform polystyrene standard; Rh 0%.

Table S14. Mean elastic modulus in GPa.

Table S15. Skewness of the elastic modulus histograms.

Fig. S4. Regression test between the thickness of the coatings and the elastic modulus.

Table S16. Are the slopes of the linear regression between the thickness of the coatings and the elastic modulus significantly different than zero?

5. Optical imaging

Fig. S5 Example photographs of wafers coated with polystyrene films.

Fig. S6. Optical microscope images of the coatings prepared from the uniform solutions 20 kDa, 90 kDa and 200 kDa or the bimodal solutions: 75/25, 50/50 or 25/75 w/w %; humidity 45% or 55%.

Fig. S7. Optical microscope images of the coatings prepared from the uniform solutions with molecular weight of polystyrene: 20 kDa, 90 kDa and 200 kDa, respectively; humidity Rh 75%.

Fig. S8. Optical microscope images of the bimodal coatings prepared from 20 kDa and 200 kDa blends, humidity 75%, molecular weight ratio w/w: 75/25, 50/50 and 25/75, respectively.

Fig. S9. Radially averaged Powers Spectra Density of coatings images, comparison between coatings made from different ratios of 20 kDa and 200 kDa polystyrene at humidity Rh 75%. Spectra were made by averaging 4 images.

6. Fourier Transform IR spectroscopy

Fig. S10. Fourier Transform IR spectra of 90 kDa and 200 kDa coatings on SiO₂. Compositions 75/25, 50/50 and 25/75 w/w % were investigated.

Fig. S11. Fourier Transform IR spectra of 20 kDa and 200 kDa coatings on SiO₂. Compositions 75/25, 50/50 and 25/75 w/w % were investigated.

Fig. S12. FTIR spectra of SiO₂ wafer.

7. Free Surface Energy and contact angle

Fig. S13. Contact angle on 20 kDa and 200 kDa uniform coatings.

Fig. S14. Free Surface Energy of 20 kDa and 200 kDa coatings. Polar and dispersive components.

8. Varying the spin-coating time

Fig. S15. PS 20 kDa and 200 kDa blend, 75/25 ratio, Spin-coating time: 0.5s and 1s

1. Experimental setup the custom build spin-coater with humidity-controlled chamber and in-situ reflectometer utilizing stroboscopic effect.

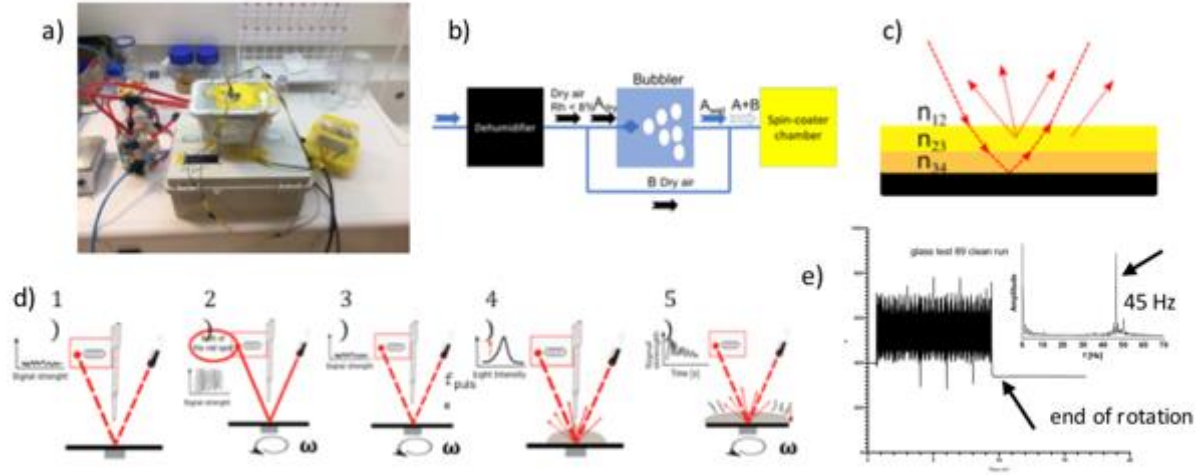


Fig S1. a) DIY spin-coater with humidity controller; b) Scheme of the humidity controller; c) illustration of the path of the light passing through multiple layers, part of the light is being scattered, n_{12} , n_{23} , n_{34} - the refractive index; d) illustration of the stroboscopic effect on filtering out the undesirable signal; e) unfiltered signal and its Fast Fourier Transform, the frequency is exact 45 Hz (equal to 2700 rpm); (Image processing software: Inkscape v0.92, <https://inkscape.org>; GraphPad Prism 9, <https://www.graphpad.com/scientific-software/prism/>)

Fig. S1 illustrates the costume setup used for the experiment is depicted in Fig. S1 a) shows picture of the experimental setup. The spin-coater, was build according to Ref. [[1]]. A custom Arduino code was written to control the spin-coater. Fig. S1 b) shows the humidity controller. The ambient air flows into the dehumidifier. The dry air flow is split, part of it flows through the bubbler to take up moisture. Regulation of the ratio between the dry and the moist air allows to sustain the desirable humidity. The mixed wet and dry air flows into the spin-coater chamber. During presented experiment, only dry air was allowed to flow into the chamber. The humidity sensor inside the chamber measured the relative humidity (Rh). The sensor indicated the relative humidity $Rh = 0\%$.

The system built for the investigation of the evaporation of the solvent during the spin-coating consisted of the Arduino microcontroller, the red laser diode ($\lambda = 650\text{nm}$, 5mW) and light dependent resistor (LDR, Velleman VMA407). A custom Arduino code was written. The

resistance of the LDR changes with the intensity of light that interacts with the resistor. The higher is light intensity the higher is the registered voltage.

The angle of incident of the laser light, taken from the device geometry, was around 5°. Thus, for calculations the incident beam will be treated as normal to the surface. Fig. S1c) illustrates light passing through the multiple layers that have got different refractive indexes n_{ij} . The refractive index n of the solution can be calculated from:

$$n_{mix} = \frac{m_p n_p + m_s n_s}{m_p + m_s},$$

where m_i and n_i is molecular mass and refractive index of polymer and solvent respectively.[2].

For the MEK/PS system the refractive index can be assumed as $n = 1.4$, while for the MEK the refractive index is $n = 1.38$ and for PS the refractive index is $n = 1.5$.

The position of the laser diode, the LDR, sample and the pipet with the solution is depicted in Fig. S1 d) 2) illustrates that the sample wobbles during the rotation. In result, the graph presenting the signal shows fringes with frequency corresponding with the rotational speed of the sample rotation. To overcome this technical problem, the Arduino was programmed to utilize the stroboscopic effect. The laser diode and LDR were turned on and off with frequency corresponding with the rotational speed. Fig. S1 d) 3) shows that the applied algorithm filters the unwanted signal. Fig. S1 d) 4) shows that, when the solution is pipeted onto the wafer, the laser light is scattered and the signal reading increases. Fig. S1 d) 4) shows that when the thickness of the layer of the spin-coated solution is decreasing, fringes occur in the LDR reading in the function of time. The fringes are due to the interference between light reflected from the top of the layer and the bottom of the layer.

In Fig. S1 e) graph presents actual signal reading during spinning the clean SiO wafer, without the filtering with the stroboscope algorithm and the Fast Fourier Transform (FFT) of that signal. The main peak The main peak at 45 Hz shows that the spin-coater was properly calibrated and the rotation speed was in fact 2700 rpm.

For the test of the in-situ evaporation measurement set of solvents was used. In Fig. S2 a) 35 μ l of methyl ethyl ketone (MEK) was dropped on the wafer and spun with frequency of 45 Hz (2700 rpm). The LDR voltage amplitude is presented as a function of time. Fig. S2 b) presents the measured voltage amplitude, when the clean wafer was rotating. As it can be seen, the fringes from the wobbling of the sample, seen in Fig. S1 e), were filtered out. Small amplitude jump is seen, it marks the start of the rotation, the spin-coater needs time to accelerate. During acceleration the device and the spin-coater are out of phase. This period is short and lasts around 0.2 s.

The curve showing the evaporating of MEK as seen in Fig. S2 a) consist of two regions. First, during which interference fringes can be seen, lasts 0.92 s. The second phase lasts until 5.89 s and depicts the end of the MEK film evaporation. This is with agreement with results found in the literature. [3] The first phase is often depicted as the “hydrodynamic thinning”, while the following phase is referred as “solvent thinning” phase.

The difference in length of the light path reflected from the top and bottom of the optical layer result in the interference between these two beams of light. The condition for minimum and maximum of the interreference fringes can be taken from Bragg’s equation: $2nd \cos\theta = m\lambda$, where n is the refractive index of the layer, d is thickness of the layer, θ – incident angle, m is integer and λ is wavelength. The distance between two interference maximums is $\Delta d = 235$ nm (refractive index of MEK $n_{\text{MEK}}=1.3788$). In case of solution of PS in MEK the refractive index is assumed to be 1.5 and the Δd is 217 nm. The interference fringes can occur only if the layer is thinning and its thickness is more than Δd . If the thickness of the layer drops below the Δd , the next fringes would not appear. Moreover, as the film becomes thinner the amount of scattered light decreases as $I_s \sim I_0 \exp[-d]$, it can be assumed that the signal output will decrease with time of the spin-coating.

The rate of evaporation of the solution during spin-coating can be defined as the difference between first and last interference fringes.

The total evaporation rate $R = \Delta t / V_{\text{solution}}$.

And the thinning rate of the film created by the spin-coated solution is:

The thinning rate $dh/dt = \Delta d / \Delta t$.

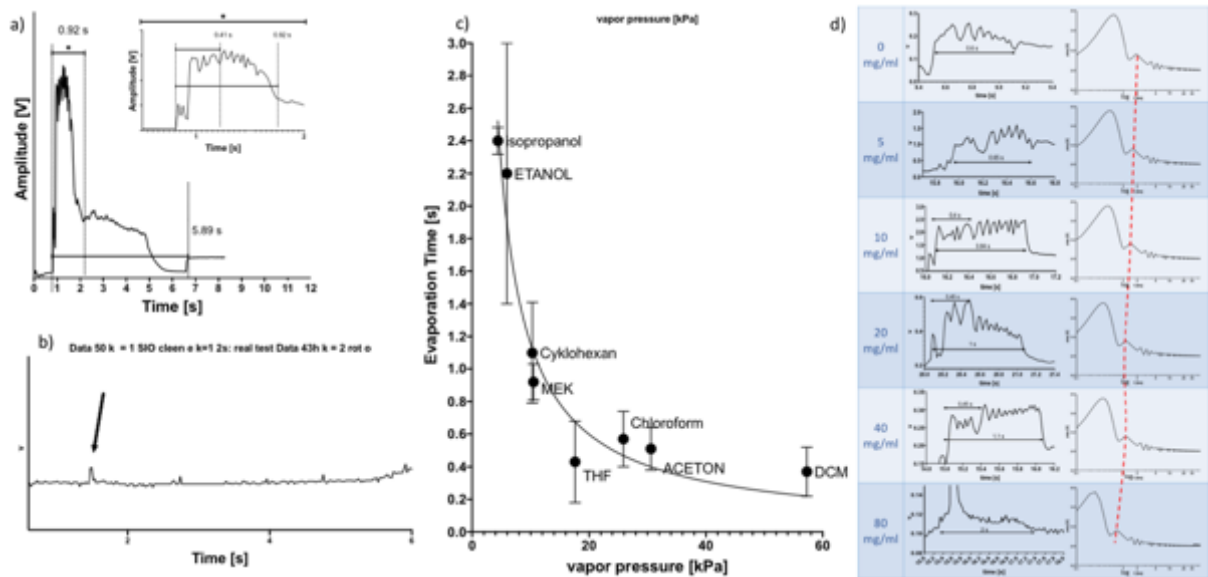


Fig. S2 a) Intensity of the light measured as a LDR voltage [V] in function of time [s] during spin-coating 35 μ l of MEK; b) reference signal obtained during the rotation of the clean SiOx wafer; c) graph presents the evaporation times for different test solvents; d) graphs obtained for the increasing concentration of PS in MEK, and the corresponding Fast Fourier Transforms of the signals; (Image processing software: PowerPoint 365, <https://office.live.com>; GraphPad Prism 9, <https://www.graphpad.com/scientific-software/prism/>)

Fig. S2 c) shows the evaporation time between first and last fringe for different solvents plotted as function of their vapor pressure. The fitting curve is power series in form of $A \cdot X^B + C \cdot X^D$. As can be seen, the evaporation rate of solvent with similar vapor pressure are similar, i.e. cyclohexane and MEK.

Fig. S2 d) shows the evaporation curves for the mixture of polystyrene with MEK in different concentrations c. Corresponding Fast Fourier Transforms (FFT) of the signals are shown. The second frequency corresponds to the duration of the fringes. The progressive shift towards the lower frequencies shows increasing duration of the fringes in respect to the polymer concentration. Thus, the rate of the evaporation can be retrieved from the FFT analysis.

2. Film thickness analysis.

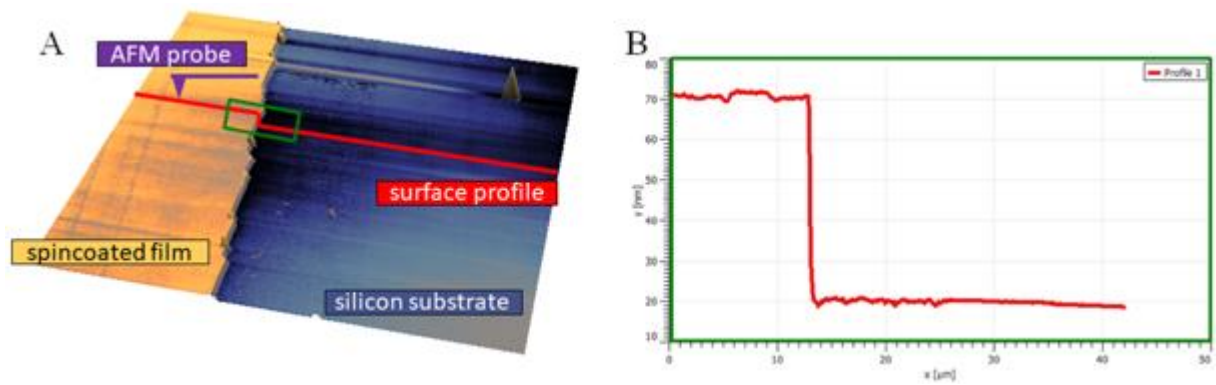


Fig S3. A) Schematic illustration of spin-coated film's thickness assessment, B) Representative topographical profile a sample recorded using AFM. (Image processing software: PowerPoint 365, <https://office.live.com>; Gwyddion v2.50, <http://gwyddion.net/>)

3. Viscosity analysis

Table S1. Coefficients K and $[\eta]$ for relation between viscosity and concentration, $\frac{\eta_r}{c} = [\eta](1 + K[\eta]c + \frac{(K[\eta]c)^2}{2} + \frac{(K[\eta]c)^3}{6})$; 95% confidence interval CI; goodness of the fit coefficients: R^2 and sum of squares SS.

	$[\eta]$	K	95% CI		Fit quality	
			$[\eta]$	K	R^2	SS
Uniform 20	0.012	0.33	0.006 to 0.020	-0.66 to 2.71	0.022	0.0027
Uniform 91	0.048	0.10	0.037 to 0.060	-0.01 to 0.26	0.215	0.0032
Uniform 150	0.035	0.40	0.025 to 0.046	0.21 to 0.76	0.758	0.0029
Uniform 200	0.052	0.36	0.046 to 0.058	0.29 to 0.46	0.975	0.0017
75/25**	0.013	1.01	0.011 to 0.015	0.70 to 1.46	0.922	0.0001
50/50**	0.029	0.40	0.026 to 0.031	0.32 to 0.49	0.934	0.0004
25/75**	0.026	0.93	0.017 to 0.035	0.55 to 1.77	0.919	0.0028
75/25*	0.018	1.36	0.013 to 0.023	0.89 to 2.25	0.940	0.0014
50/50*	0.033	0.54	0.030 to 0.036	0.46 to 0.63	0.986	0.0003
25/75*	0.035	0.61	0.029 to 0.040	0.47 to 0.81	0.973	0.0020

* - Blends of 91 kDa and 200 kDa polystyrene; ** - blend of 20 kDa and 200 kDa polystyrene; x/x – w/w% ratio of blended uniform polystyrenes.

Table S2. Coefficients for Mark-Houwink equation.

	c 80 [mg/ml]	c 40 [mg/ml]	c 20 [mg/ml]	c 10 [mg/ml]
Uniform				
K	-10.29	-8.23	-5.86	-5.72
CI 95%	-13,28 to -8,03	-12,30 to -5,84	-9,69 to -3,84	-7,04 to -4,75
a	1.65	1.13	0.60	0.55
CI 95%	1,21 to 2,22	0,66 to 1,91	0,18 to 1,35	0,35 to 0,81
R ²	0,953	0,895	0,510	0,841
SS	0,004	0,002	0,005	0,001
Bimodal				
K	-10.09	-9.99	-7.53	-11.16
CI 95%	-10,97 to -9,26	-11,22 to -8,88	-8,80 to -6,35	-18,89 to -5,67
a	1.62	1.47	0.87	1.58
CI 95%	1,45 to 1,79	1,25 to 1,72	0,631 to 1,13	0,463 to 3,11
R ²	0,959	0,948	0,729	0,388
SS	0,002	0,001	0,001	0,004

CI - Confidence Interval; SS - sum of squares.

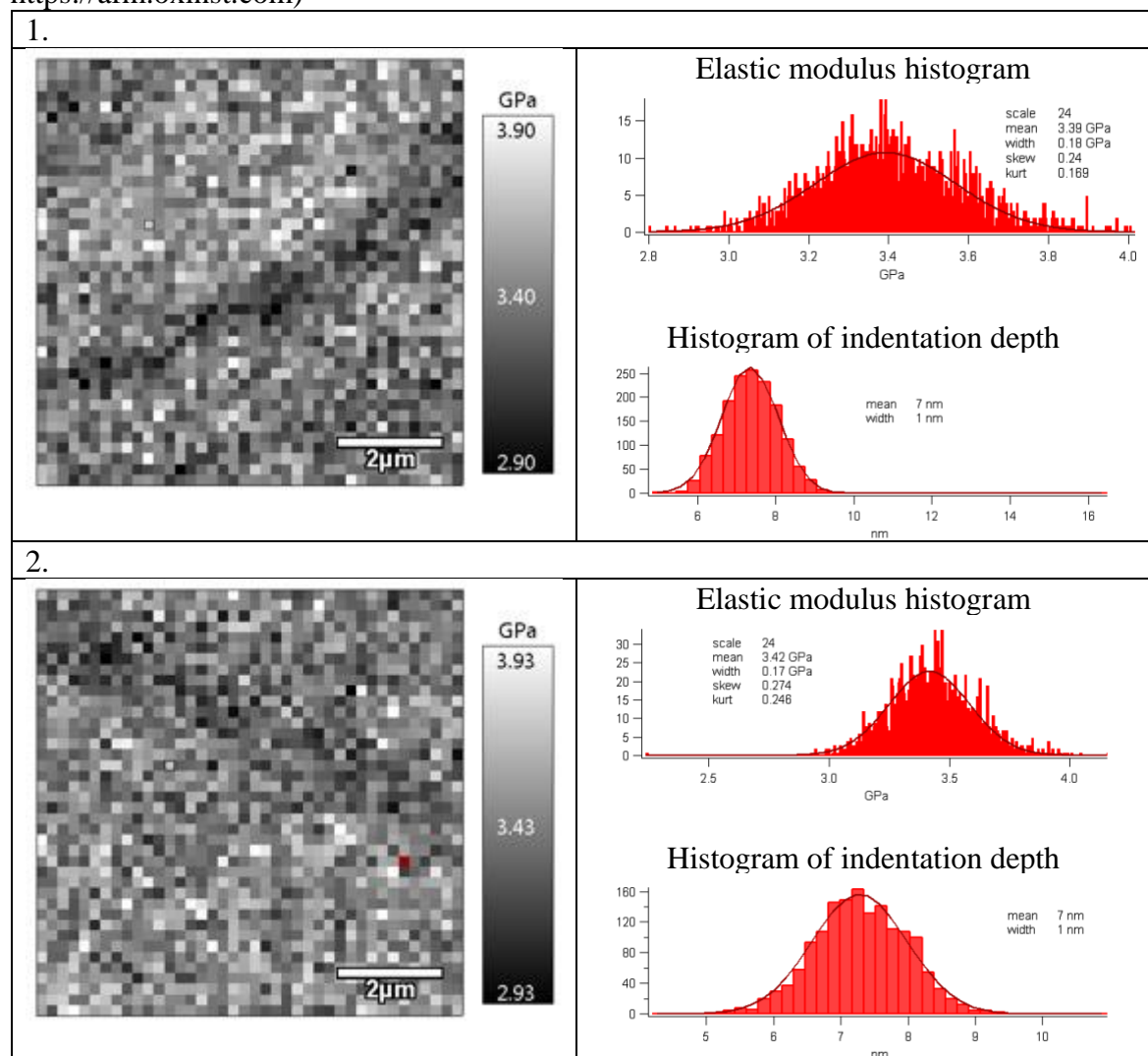
Table S3. Dynamic viscosity values of the uniform solutions in cP. Viscosity of Pure MEK: 0.39 ± 0.04 cP.

1. Uniform						
Concentration [mg/ml]	PS 20 kDa	PS 90 kDa	PS 150 kDa	PS 200 kDa		
5	0.39 ± 0.04	0.49 ± 0.05	0.48 ± 0.04	0.50 ± 0.05		
10	0.39 ± 0.04	0.55 ± 0.05	0.58 ± 0.03	0.63 ± 0.03		
20	0.45 ± 0.01	0.85 ± 0.11	0.64 ± 0.10	0.99 ± 0.07		
40	0.59 ± 0.02	1.22 ± 0.04	1.34 ± 0.24	2.15 ± 0.07		
80	0.95 ± 0.02	2.60 ± 0.55	3.73 ± 0.24	7.18 ± 0.25		
2. Bimodal						
Concentration [mg/ml]	20 kDa and 200 kDa blend			90 kDa and 200 kDa blend		
	75/25	50/50	25/75	75/25	50/50	25/75
5	0.42 ± 0.01	0.46 ± 0.02	0.43 ± 0.02	0.43 ± 0.01	0.46 ± 0.01	0.44 ± 0.01
10	0.44 ± 0.01	0.53 ± 0.02	0.57 ± 0.10	0.43 ± 0.01	0.57 ± 0.02	0.55 ± 0.05
20	0.53 ± 0.01	0.66 ± 0.03	0.66 ± 0.02	0.65 ± 0.05	0.75 ± 0.03	0.78 ± 0.01
40	0.78 ± 0.02	1.09 ± 0.05	1.47 ± 0.03	1.24 ± 0.05	1.39 ± 0.05	1.88 ± 0.02
80	1.52 ± 0.03	2.63 ± 0.12	5.14 ± 0.32	3.72 ± 0.26	4.45 ± 0.04	5.69 $0,15$

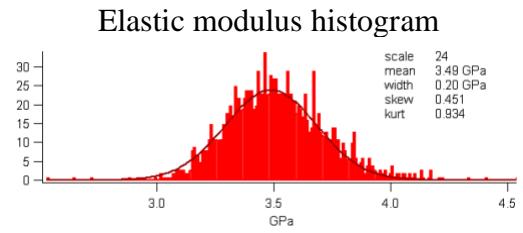
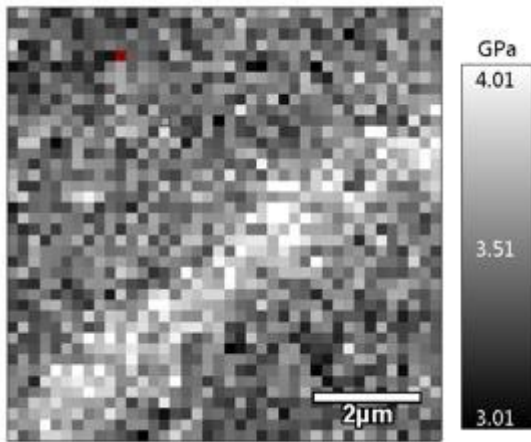
4. Force Spectroscopy

The blends were prepared by spin coating the polystyrene blend solution on a SiO_x wafer. Force maps were prepared using AFM force spectroscopy. Each point on the map represents the value of the elastic modulus at that point. Humidity during spinning was kept close to 0%. All force maps are scaled to the same range as follows: mean \pm 1 GPa. All elastic modulus histogram bins were scaled to the same scale.

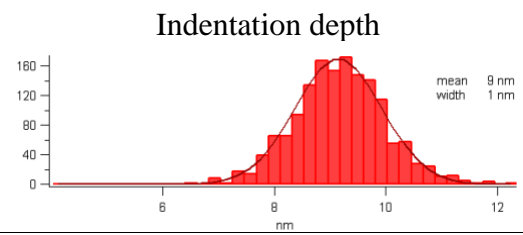
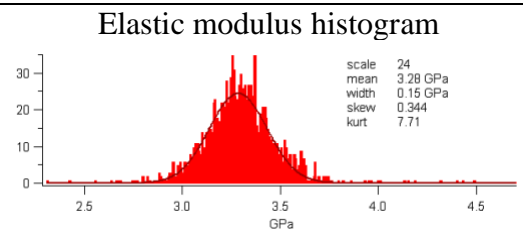
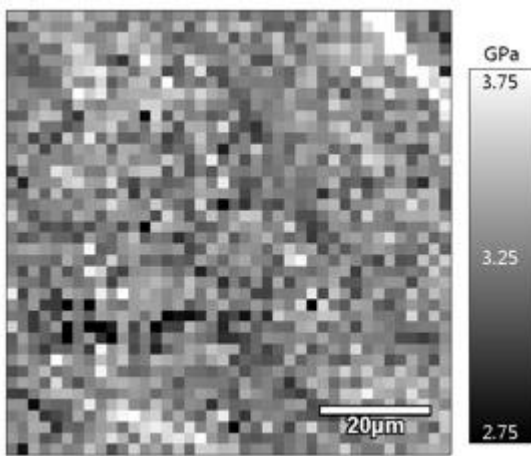
Table S4. Blend of 20 kDa and 200 kDa polystyrene; 75/25 w/w%; Rh 0%. (Image processing software: Igor Pro 6.37 with Asylum Research 15.02.105 add-on, <https://afm.oxinst.com>)



3.



4.



5.

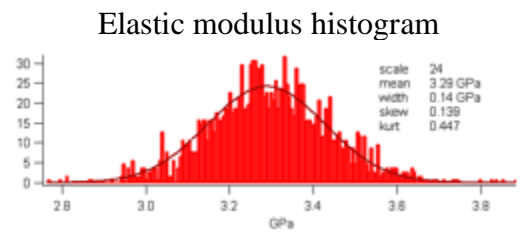
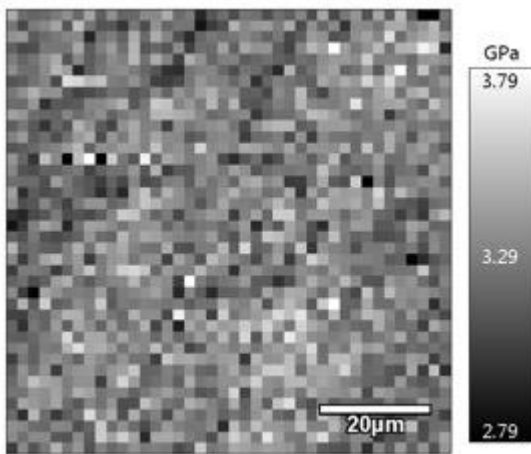


Table S5. Blend of 20 kDa and 200 kDa polystyrene; 50/50 w/w%; Rh 0%. (Image processing software: Igor Pro 6.37 with Asylum Research 15.02.105 add-on, <https://afm.oxinst.com>)

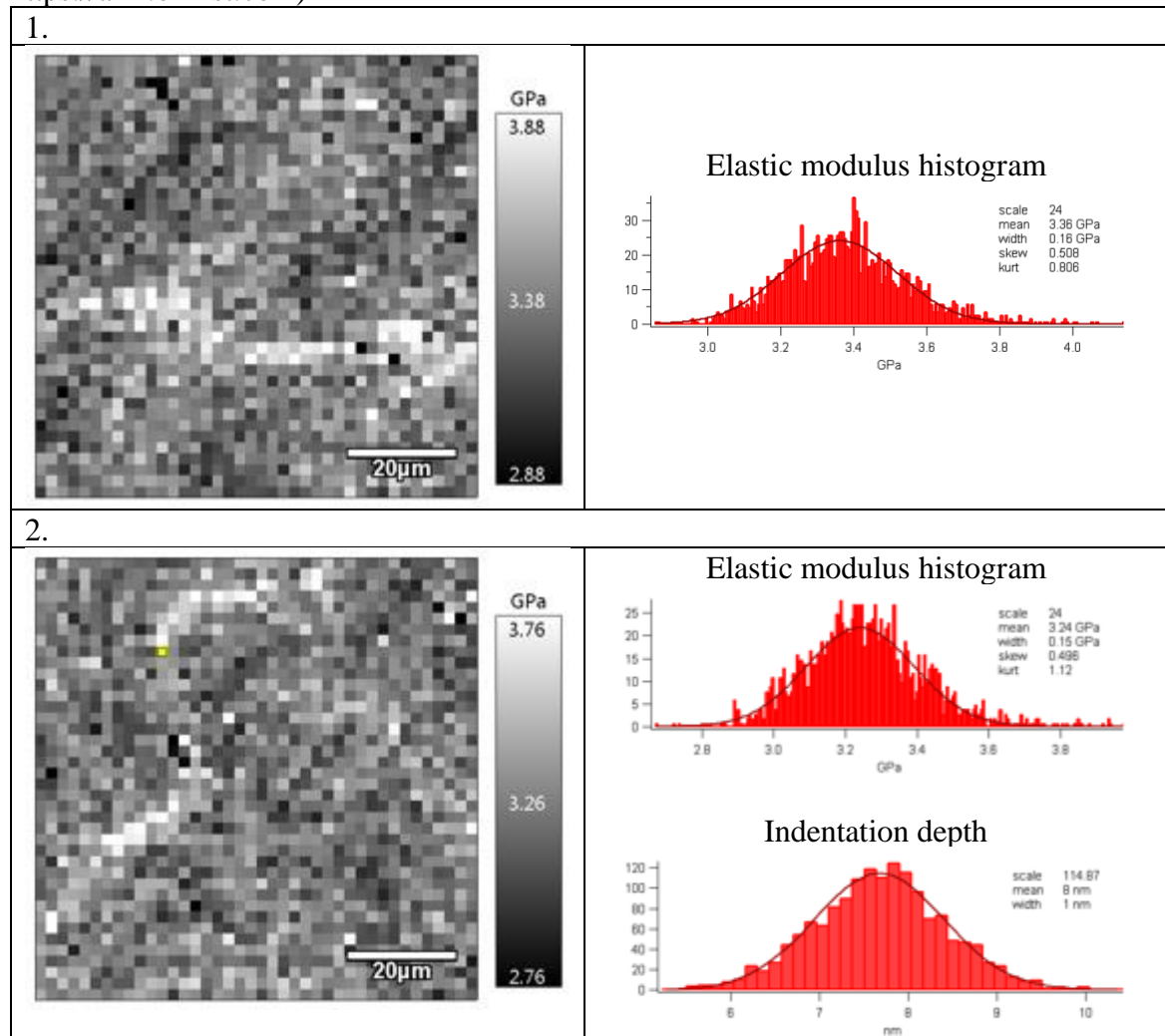
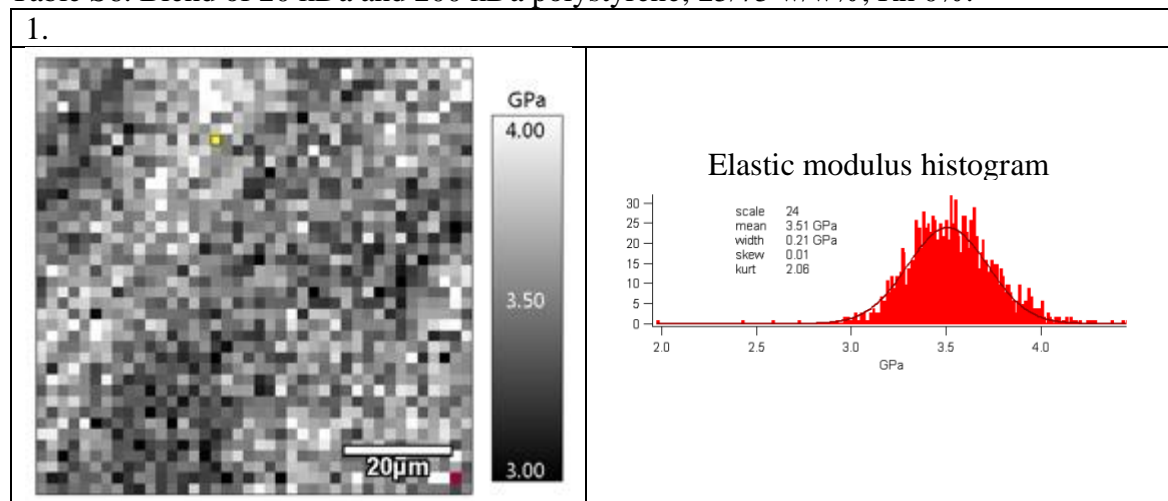
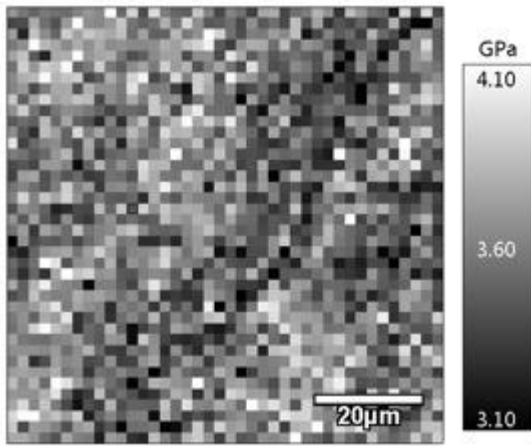


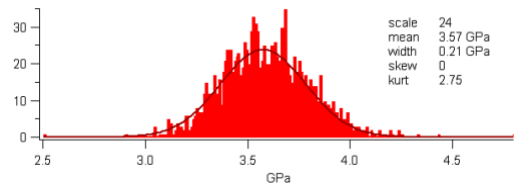
Table S6. Blend of 20 kDa and 200 kDa polystyrene; 25/75 w/w%; Rh 0%.



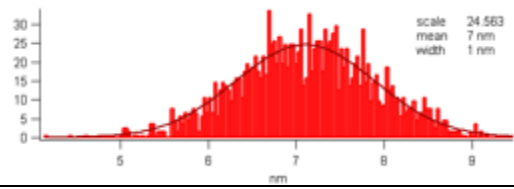
2.



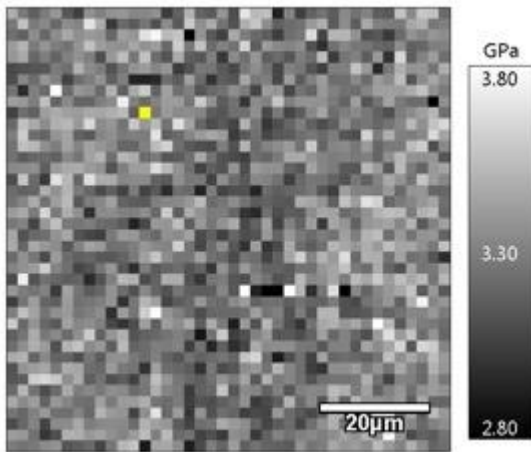
Elastic modulus histogram



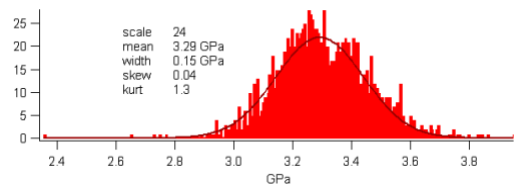
Indentation depth



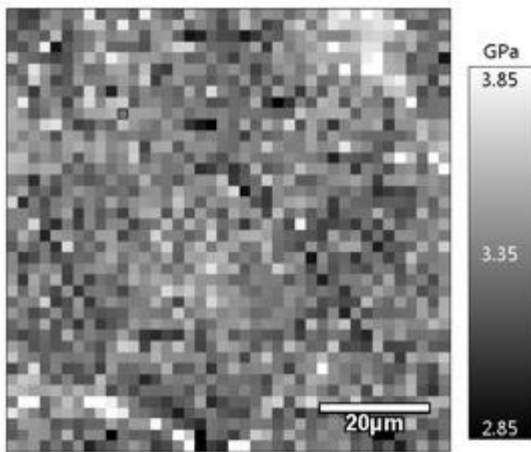
3.



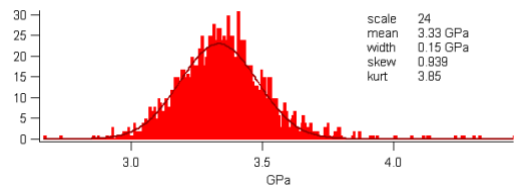
Elastic modulus histogram



4.



Elastic modulus histogram



Indentation depth

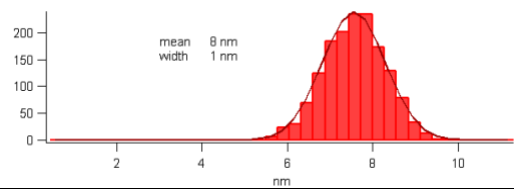


Table S7. Blend of 91 kDa and 200 kDa polystyrene; 75/25 w/w%; Rh 0%. (Image processing software: Igor Pro 6.37 with Asylum Research 15.02.105 add-on, <https://afm.oxinst.com>)

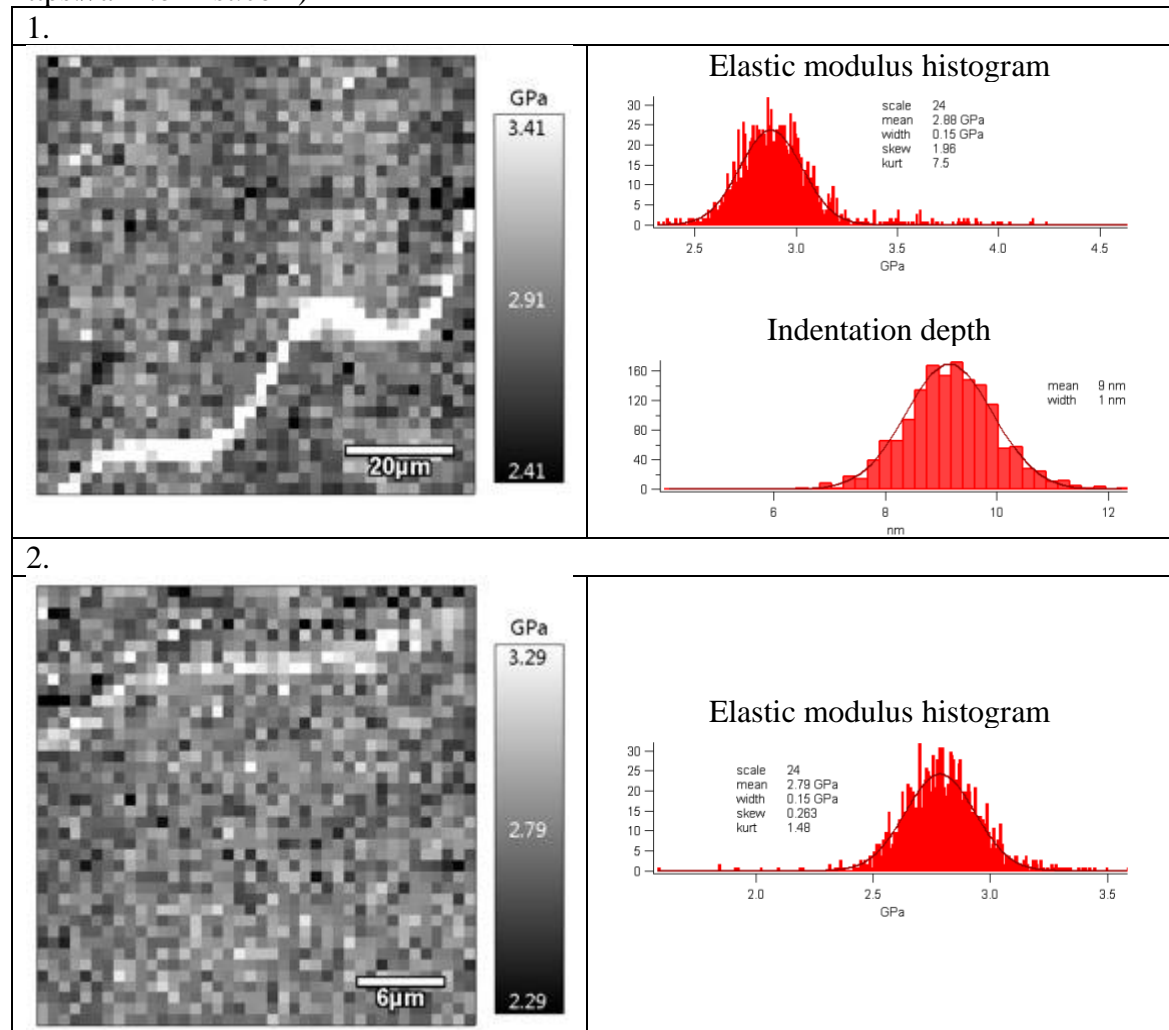


Table S8. Blend of 91 kDa and 200 kDa polystyrene; 50/50 w/w%; Rh 0%. (Image processing software: Igor Pro 6.37 with Asylum Research 15.02.105 add-on, <https://afm.oxinst.com>)

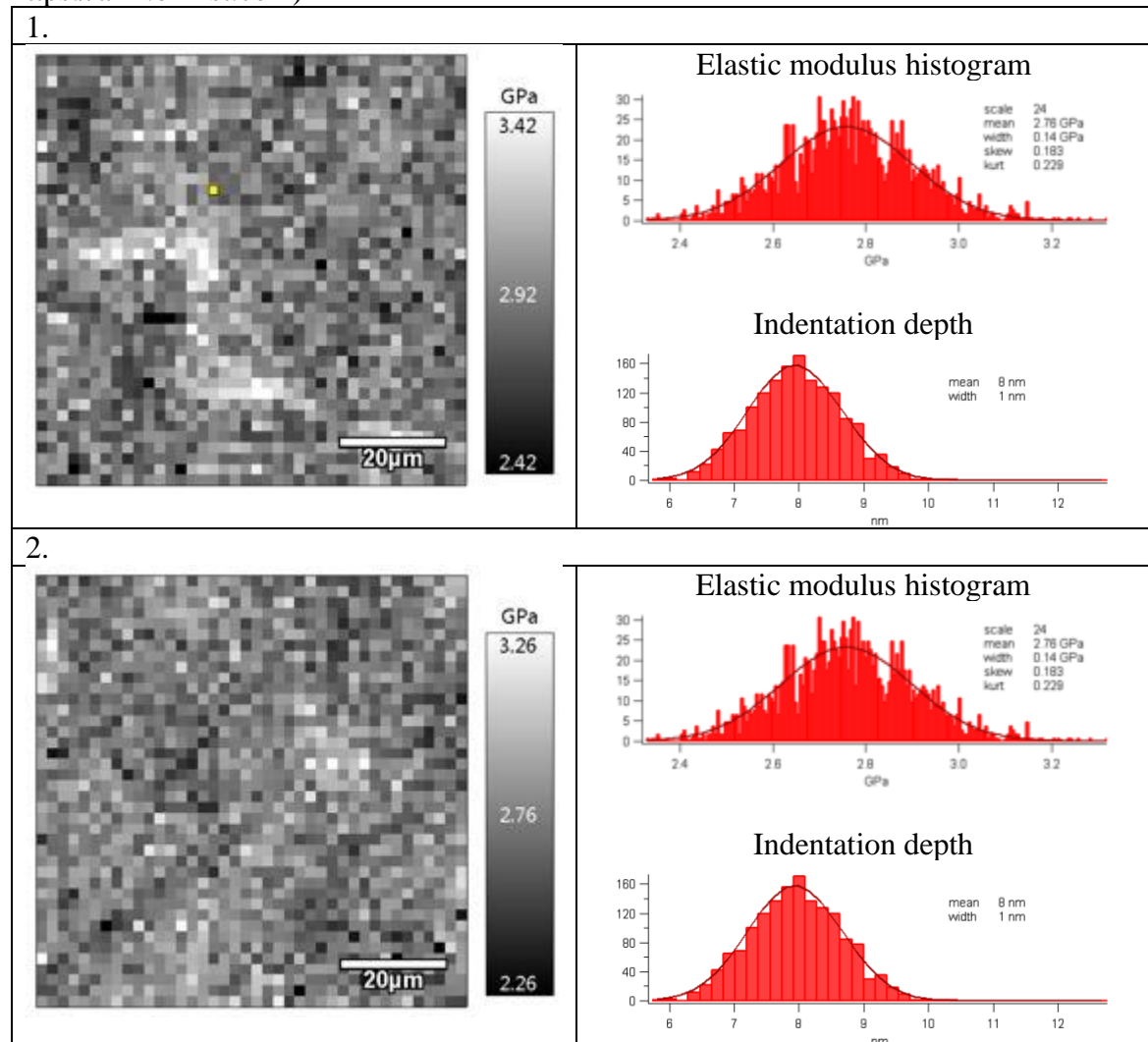


Table S9. Blend of 91 kDa and 200 kDa polystyrene; 25/75 w/w%; Rh 0%. (Image processing software: Igor Pro 6.37 with Asylum Research 15.02.105 add-on, <https://afm.oxinst.com>)

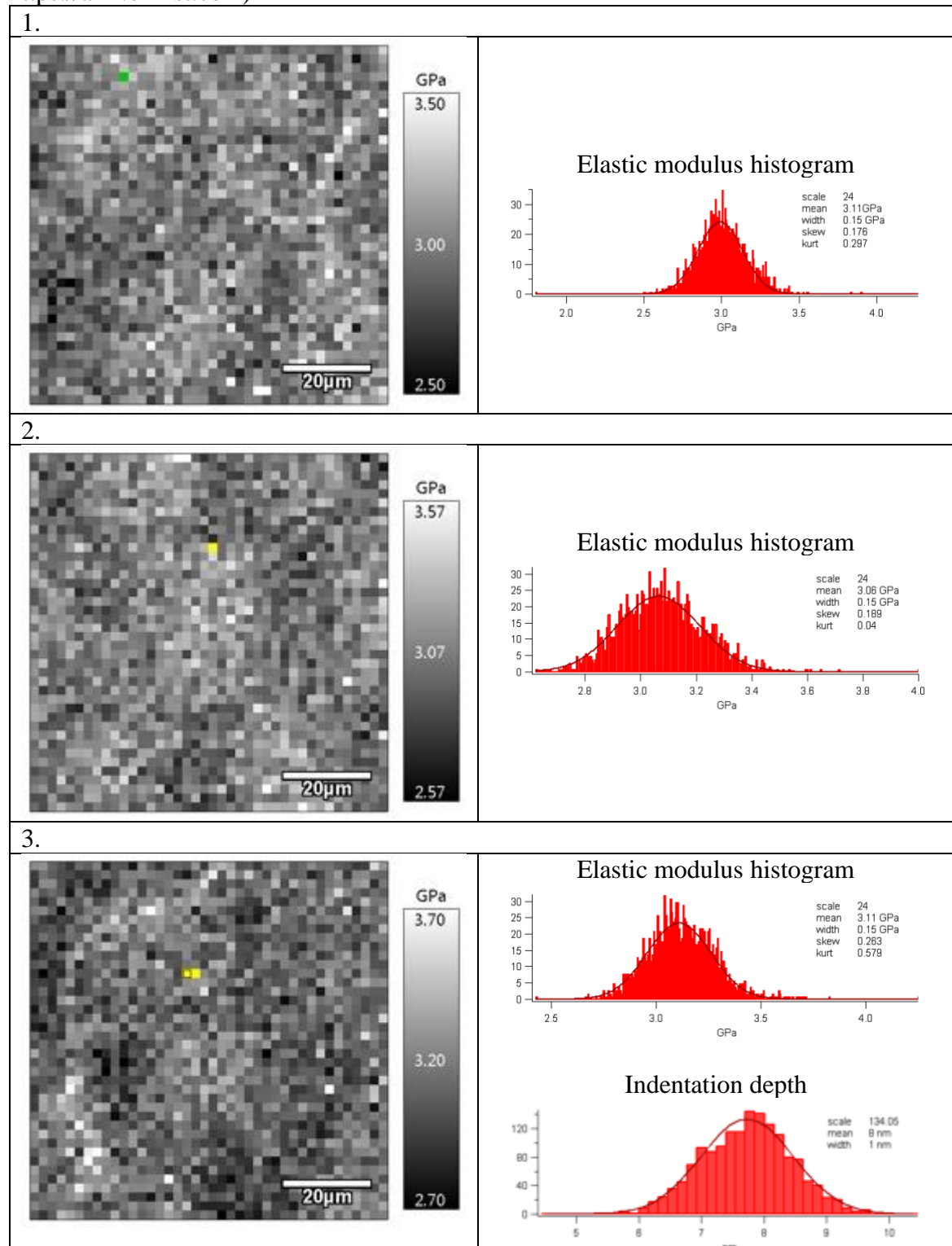
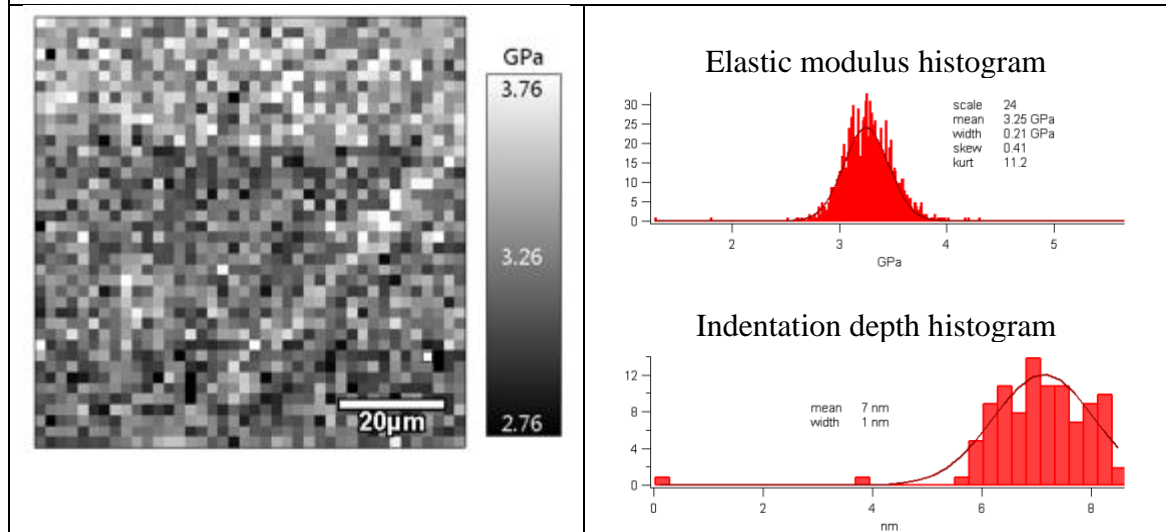


Table S10. 20 kDa uniform polystyrene standard; Rh 0%. (Image processing software: Igor Pro 6.37 with Asylum Research 15.02.105 add-on, <https://afm.oxinst.com>)

1.



2.

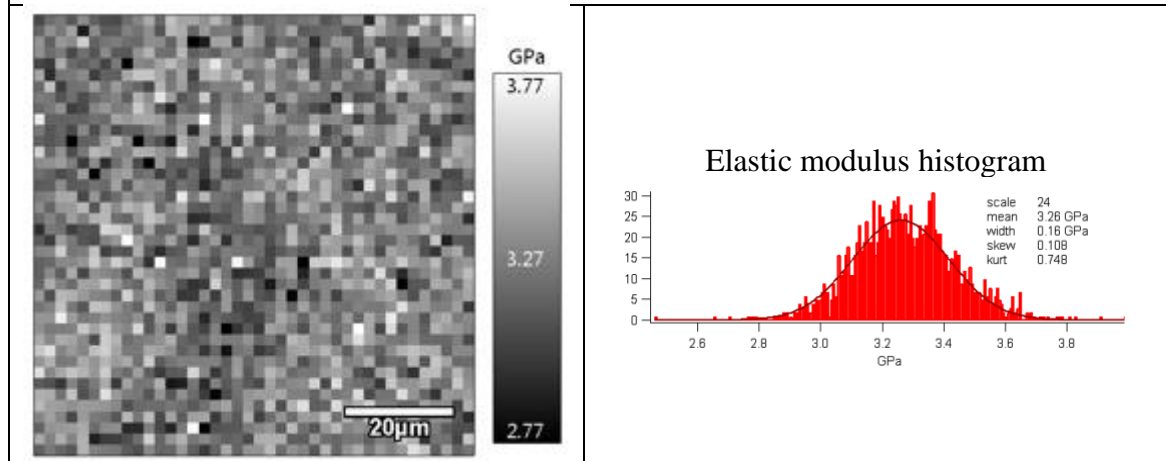
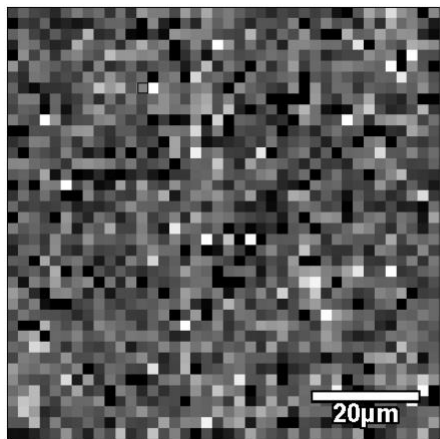
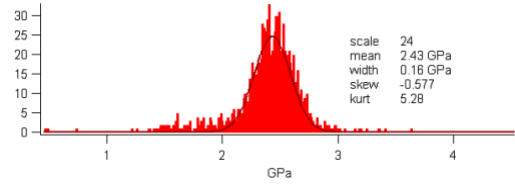


Table S11. 91 kDa uniform polystyrene standard; Rh 0%. (Image processing software: Igor Pro 6.37 with Asylum Research 15.02.105 add-on, <https://afm.oxinst.com>)

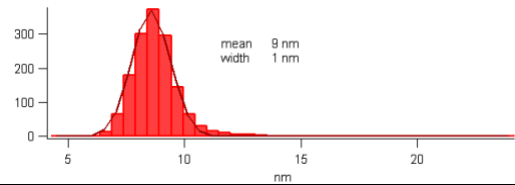
1.



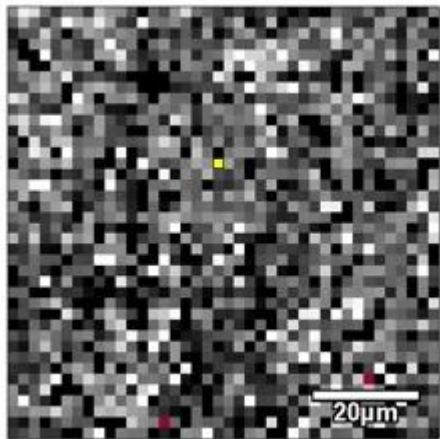
Elastic modulus histogram



Indentation depth



2.



Elastic modulus histogram

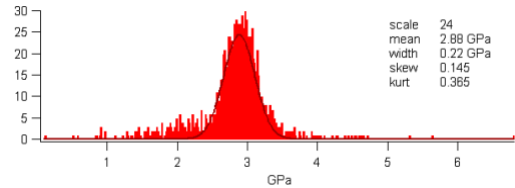


Table S12. 150 kDa uniform polystyrene standard; Rh 0%. (Image processing software: Igor Pro 6.37 with Asylum Research 15.02.105 add-on, <https://afm.oxinst.com>)

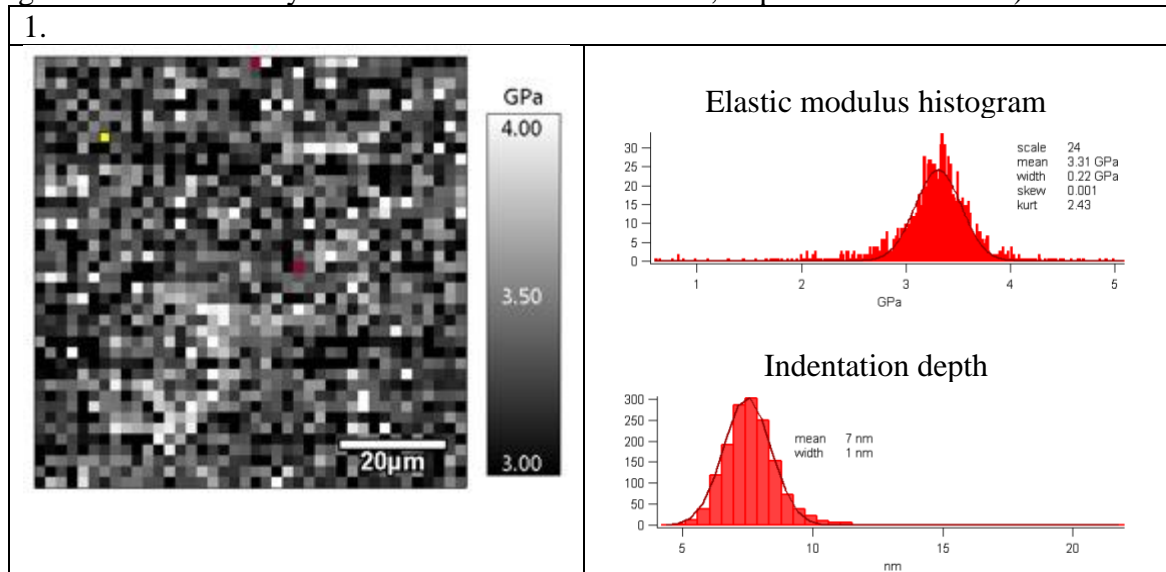


Table S13. Blend of 200 kDa uniform polystyrene standard; Rh 0%. (Image processing software: Igor Pro 6.37 with Asylum Research 15.02.105 add-on, <https://afm.oxinst.com>)

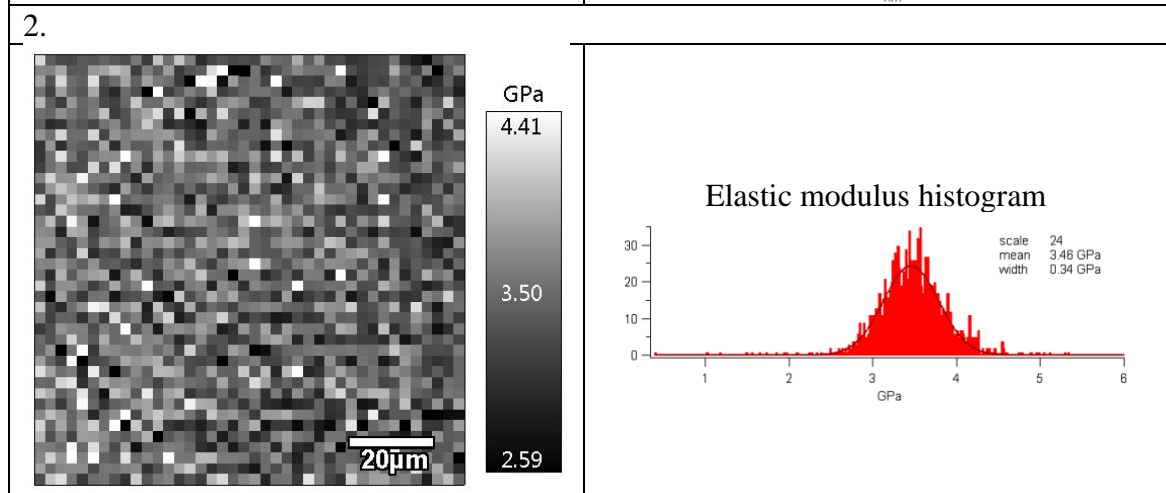
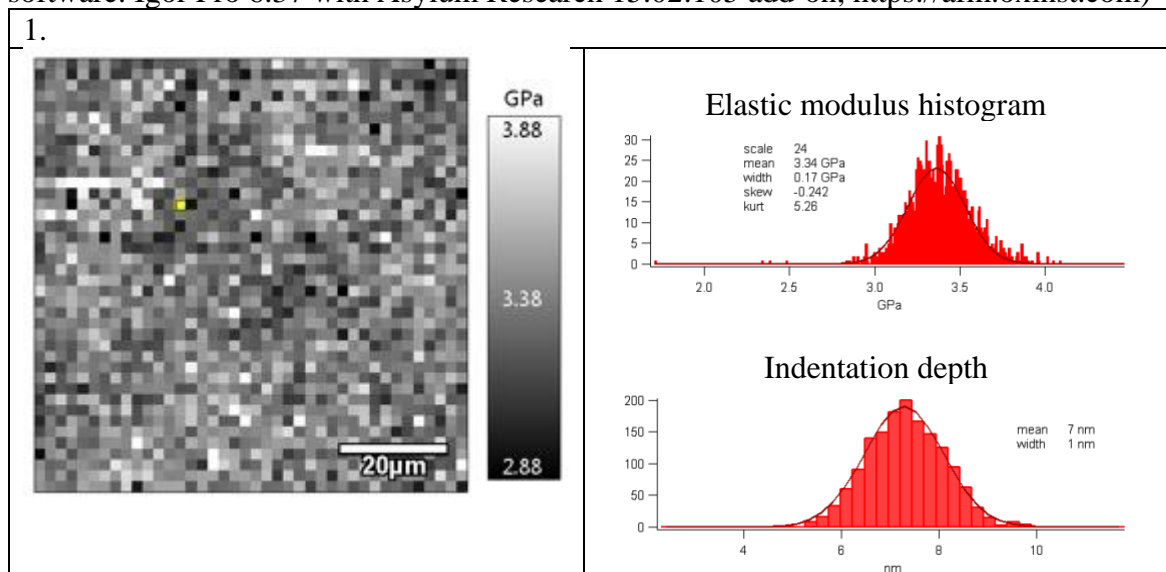


Table S14. Mean elastic modulus in GPa. The calculation takes into account all prepared force maps, including higher (images above) and low-resolution maps (images not included).

Uniform				
Type of polystyrene	PS 20 kDa	PS 91 kDa	PS 150 kDa	PS 200 kDa
Number of tests	20 [†]	8	6	6
Mean	3.271	<u>2.896</u>	3.165	3.272
Std. Deviation	0.272	0.382	0.339	0.318
Std. Error of Mean	0.061	0.135	0.138	0.130
Blend of 90 kDa and 200 kDa				
Ratio w/w%	75/25*	50/50*	25/75*	X
Number of tests	3	3	4	
Mean	<u>2.833</u>	<u>2.777</u>	3.003	
Std. Deviation	0.045	0.015	0.117	
Std. Error of Mean	0.026	0.009	0.059	
Blend of 20 kDa and 200 kDa				
Ratio w/w%	75/25**	50/50**	25/75**	X
Number of tests	7	5	6	
Mean	3,119	3,296	3,285	
Std. Deviation	0,376	0,049	0,427	
Std. Error of Mean	0,142	0,022	0,174	

Ordinary one-way ANOVA test for 10 means: the means are significantly different, $P = 0.0254$. Underlined are means significantly different ($p < 0.05$), Fisher's multiple comparisons test.
[†] 20 kDa polystyrene coatings were used as a control. After couple of tests of different coatings, the 20 kDa coating was retested to control the consistency of the experiment.
* - Blends of 91 kDa and 200 kDa polystyrene; ** - blend of 20 kDa and 200 kDa polystyrene; $x/x - w/w\%$ ratio of blended homogeneous polystyrenes. $[M_n] = f_1M_{w1} + f_2M_{w2}$, where f w/w. % ratio of polymers.

Table S15. Skewness of the elastic modulus histograms. Only higher resolution maps (map size: 40 lines x40 points, 80 μm x 80 μm) were considered.

Uniform				
Type of polystyrene	PS 20 kDa	PS 91 kDa	PS 150 kDa	PS 200 kDa
Mean	0.16	-0.76	-0.07	0.02
Std. Deviation	0.30	0.26	0.08	0.27
Blend of 90 kDa and 200 kDa				
Ratio w/w%	75/25*	50/50*	25/75*	X
Mean	0.98	0.22	0.17	
Std. Deviation	1.39	0.06	0.09	
Blend of 20 kDa and 200 kDa				
Ratio w/w%	75/25**	50/50**	25/75**	X
Mean	0.34	0,50	0.16	
Std. Deviation	0.24	0.37	0.22	

* - Blends of 91 kDa and 200 kDa polystyrene; ** - blend of 20 kDa and 200 kDa polystyrene; x/x – w/w% ratio of blended homogeneous polystyrenes. $[M_n] = f_1M_{w1} + f_2M_{w2}$, where f w/w. % ratio of polymers.

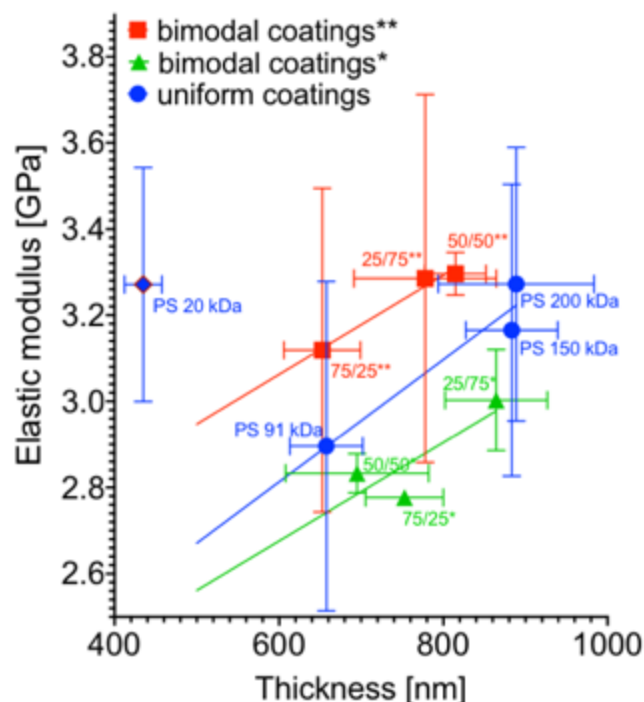


Fig. S4. Regression test between the thickness of the coatings and the elastic modulus. Uniform – coatings were made from homogeneous solutions; Bimodal – coatings made from solutions with bimodal MWD; * - Blends of 91 kDa and 200 kDa polystyrene; ** - blend of 20 kDa and 200 kDa polystyrene; x/x – w/w% ratio of blended homogeneous polystyrenes. $[M_n] = f_1M_{w1} + f_2M_{w2}$, where f w/w. % ratio of polymers. (Image processing software: GraphPad Prism 9, <https://www.graphpad.com/scientific-software/prism/>)

Table S16. Are the slopes of the linear regression between the thickness of the coatings and the elastic modulus significantly different than zero?

Type of coating	Is slope significantly non-zero?		
	Uniform	**	*
F	14.25	37.15	2.314
DFn, DFd	1, 1	1, 1	1, 1
P value	0.165	0.104	0.370
Deviation from zero?	Not Significant	Not Significant	Not Significant

* - Blends of 91 kDa and 200 kDa polystyrene; ** - blend of 20 kDa and 200 kDa polystyrene; x/x – w/w% ratio of blended homogeneous polystyrenes. $[M_n] = f_1M_{w1} + f_2M_{w2}$, where f w/w. % ratio of polymers.

5. Optical imaging.

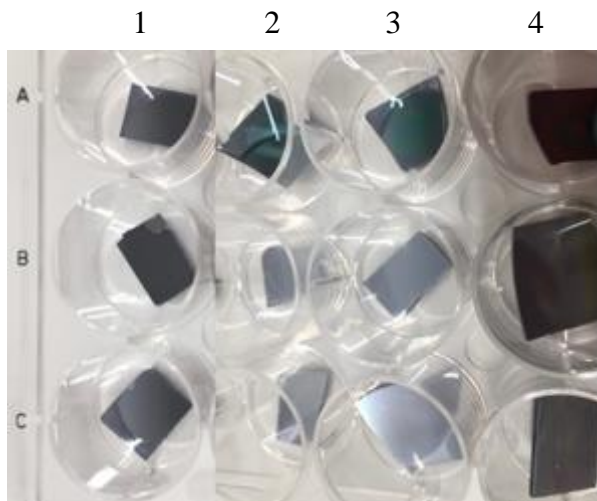


Fig. S5 Example photographs of wafers coated with polystyrene films; First Column: uniform 200 kDa coating; Rows A2 to A4: uniform 20 kDa coating; B2 – C4 – bimodal coatings, 20 kDa and 200 kDa blends; B2, C2: 25/75 w/w; B3, C3: 50/50 w/w; B4, C4: 75/25 w/w.

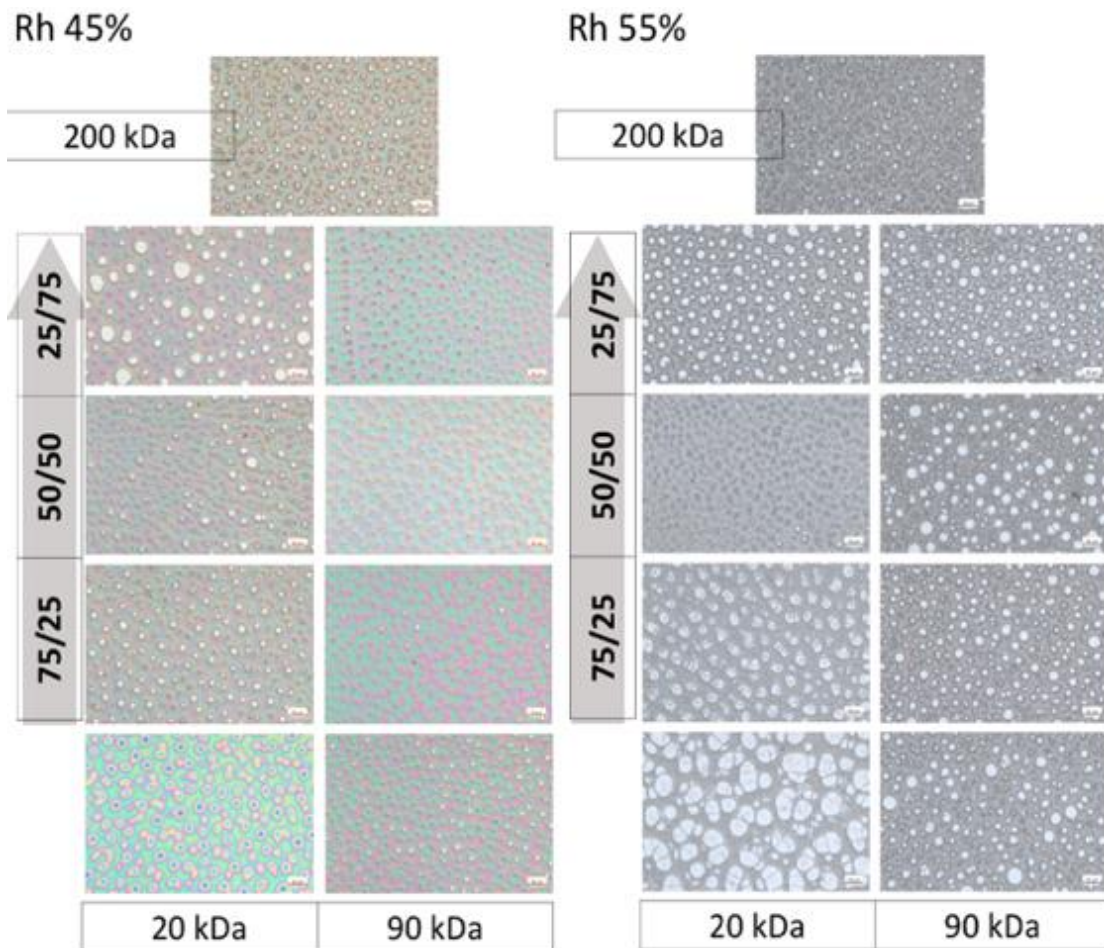


Fig. S6. Optical microscope images of the coatings prepared from the uniform solutions 20 kDa, 90 kDa and 200 kDa or the bimodal solutions: 75/25, 50/50 or 25/75 w/w %; humidity 45% or 55%. Scalebar is 50 micrometers. (Image processing software: PowerPoint 365, <https://office.live.com>)

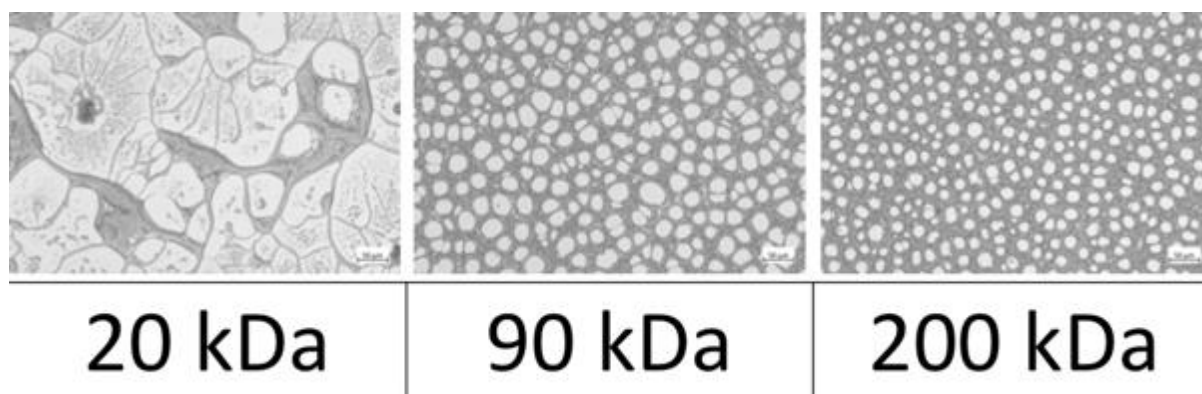


Fig. S7. Optical microscope images of the coatings prepared from the uniform solutions with molecular weight of polystyrene: 20 kDa, 90 kDa and 200 kDa, respectively; humidity Rh 75%. Scalebar is 50 micrometers. (Image processing software: PowerPoint 365, <https://office.live.com>)

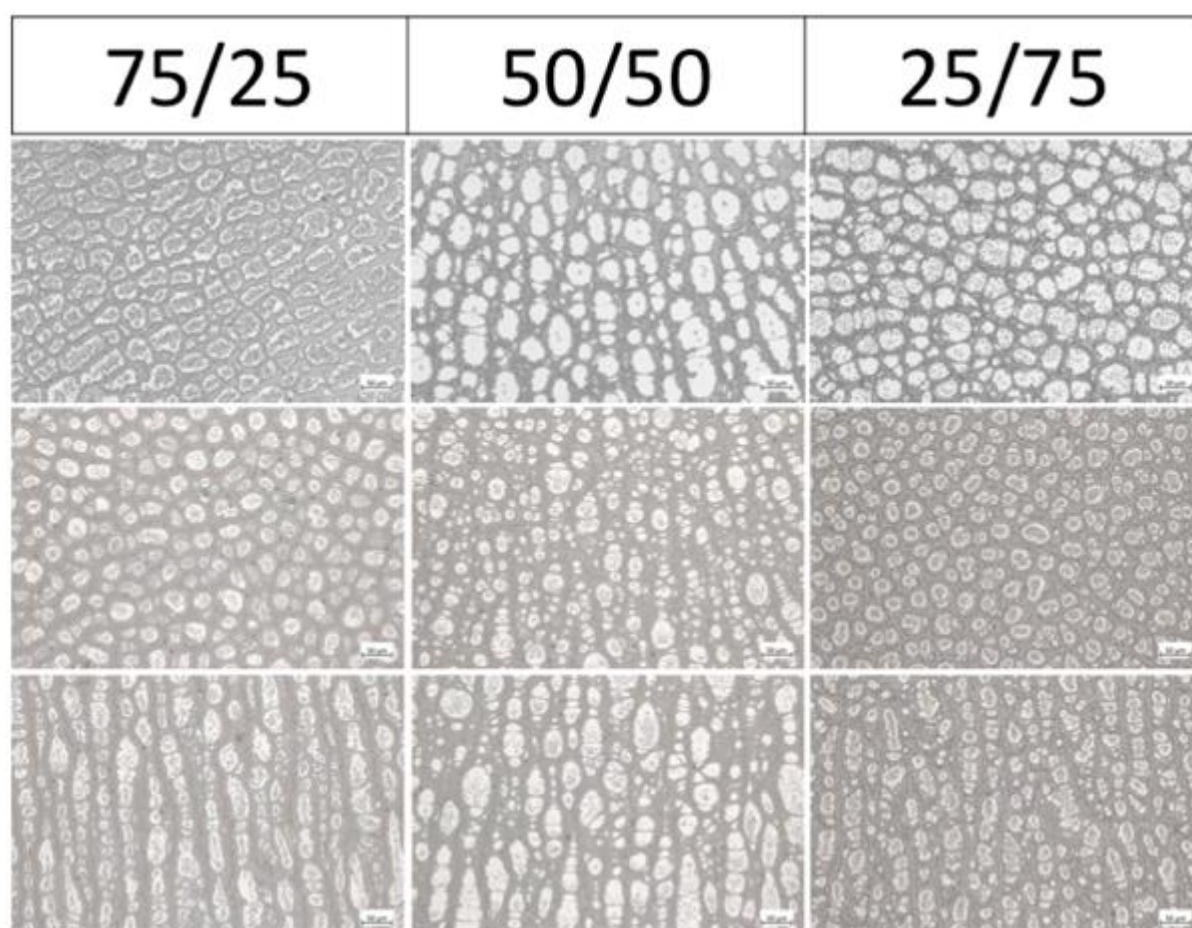


Fig. S8. Optical microscope images of the bimodal coatings prepared from 20 kDa and 200 kDa blends, humidity 75%, molecular weight ratio w/w: 75/25, 50/50 and 25/75, respectively. The first row represents a different set of samples than the next two rows. In the case of second and third two different spots of the same sample are shown in each column. Scalebar is 50 micrometers. (Image processing software: PowerPoint 365, <https://office.live.com>)

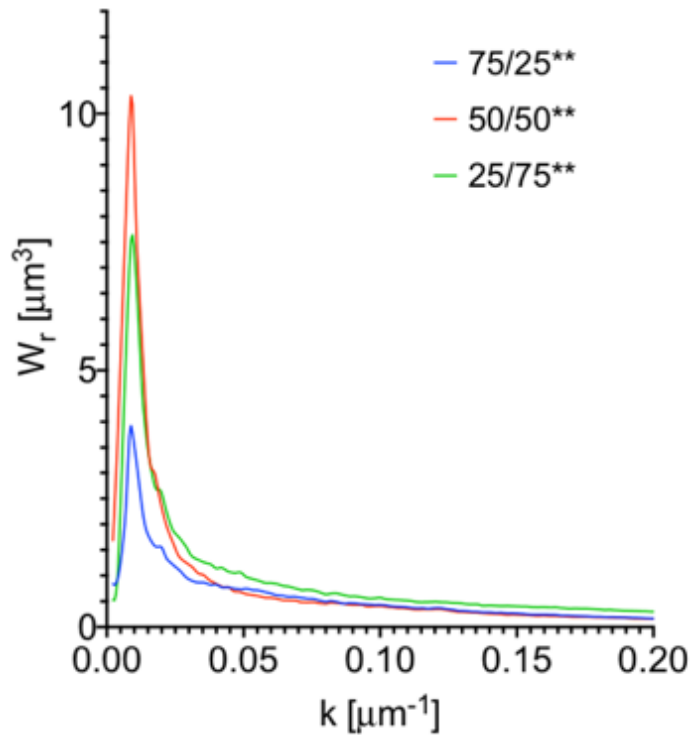


Fig. S9. Radially averaged Powers Spectra Density of coatings images, comparison between coatings made from different ratios of 20 kDa and 200 kDa polystyrene at humidity Rh 75%. Spectra were made by averaging 4 images. (GraphPad Prism 9, <https://www.graphpad.com/scientific-software/prism/>)

6. Fourier Transform IR spectroscopy of the blends

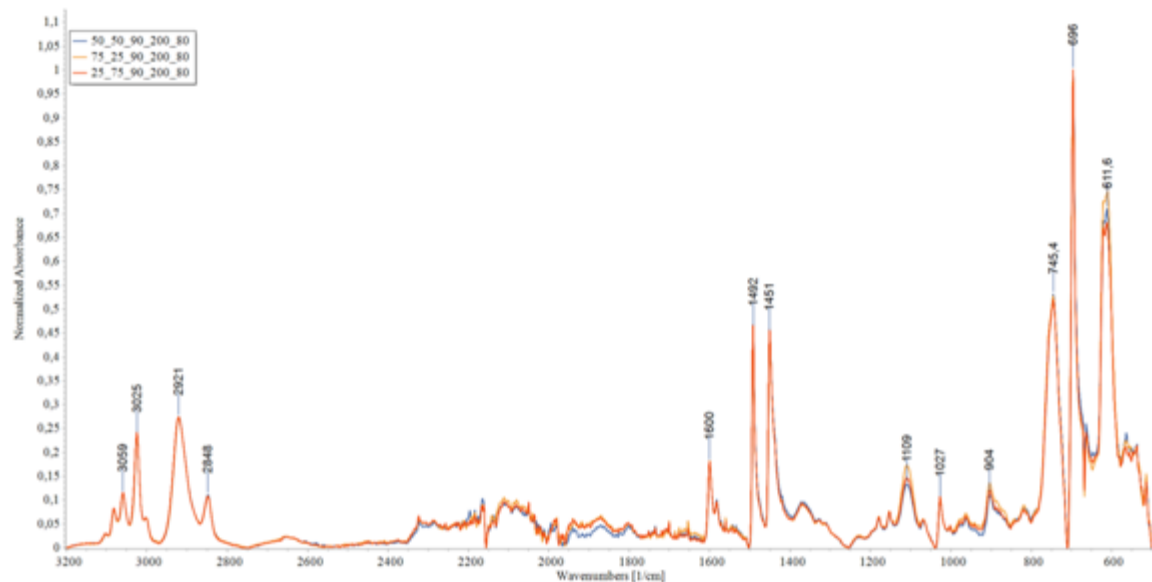


Fig. S10. Fourier Transform IR spectra of 90 kDa and 200 kDa coatings on SiO₂. Compositions 75/25, 50/50 and 25/75 w/w % were investigated. (Spectragryph v1.5.15, <https://www.effemm2.de/spectragryph/>)

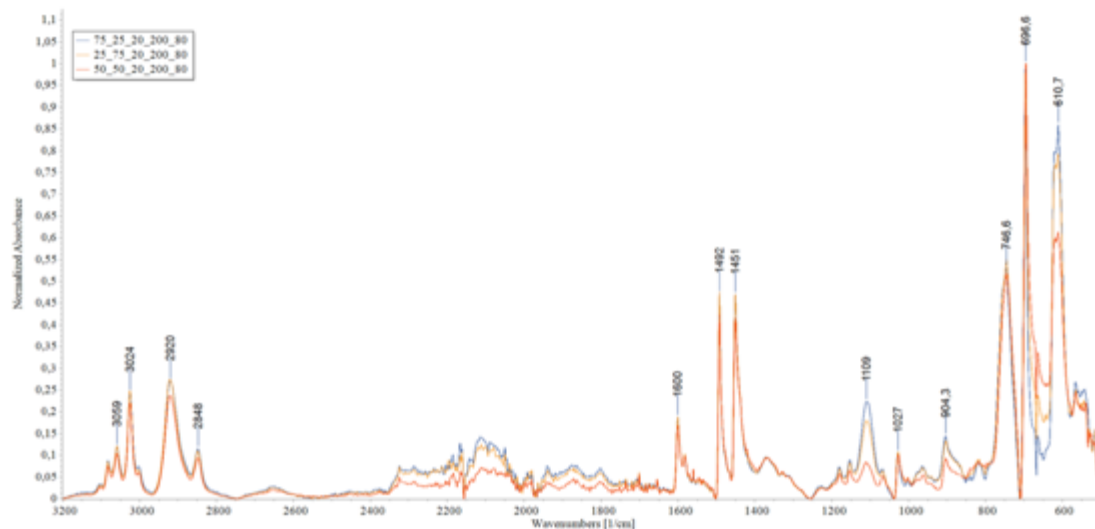


Fig. S11. Fourier Transform IR spectra of 20 kDa and 200 kDa coatings on SiO₂. Compositions 75/25, 50/50 and 25/75 w/w % were investigated. (Spectragryph v1.5.15, <https://www.effemm2.de/spectragryph/>)

Fig. S10 and Fig. S11 depicts the FTIR spectra of the 90 kDa and 200 kDa and 20 kDa and 200 kDa coatings, respectively. Coatings spun from 80 mg/ml solutions were investigated. The coatings were spun on SiO₂ wafers. The vertical axis presents normalized absorbance. The absorbance was normalized to the highest peak. The highest peak was set to 1. The recognized peaks: 3059 cm⁻¹, 3024 cm⁻¹ – benzene ring vibrations; 2920 cm⁻¹, 2848 cm⁻¹ related to -CH₃ and -CH₂ groups; 1600 cm⁻¹, 1492 cm⁻¹ – benzene ring vibrational modes, 1451 cm⁻¹: -CH and -CH₂ groups; 1027 cm⁻¹, 904 cm⁻¹ - benzene ring vibrational modes; 747 cm⁻¹ and 697 cm⁻¹ – main benzene vibrational modes; are related to polystyrene chemical structure.[4] Two odd peaks: at 1109 cm⁻¹ and 611 cm⁻¹ should be attributed to SiO₂ background as shown in Fig. S12.



Fig. S12. FTIR spectra of SiO₂ wafer. (Spectragryph v1.5.15, <https://www.effemm2.de/spectragryph/>)

It can be noticed that the intensity of the 1109 cm^{-1} and 611 cm^{-1} is related to the thickness of the films. The 20 kDa and 200 kDa 75/25 w/w % coating was the thinnest.

To summarize, spectra typical for pristine polystyrene were found. It can be concluded that the end groups were typical $-\text{CH}_3$ groups.

7. Surface free energy and contact angle

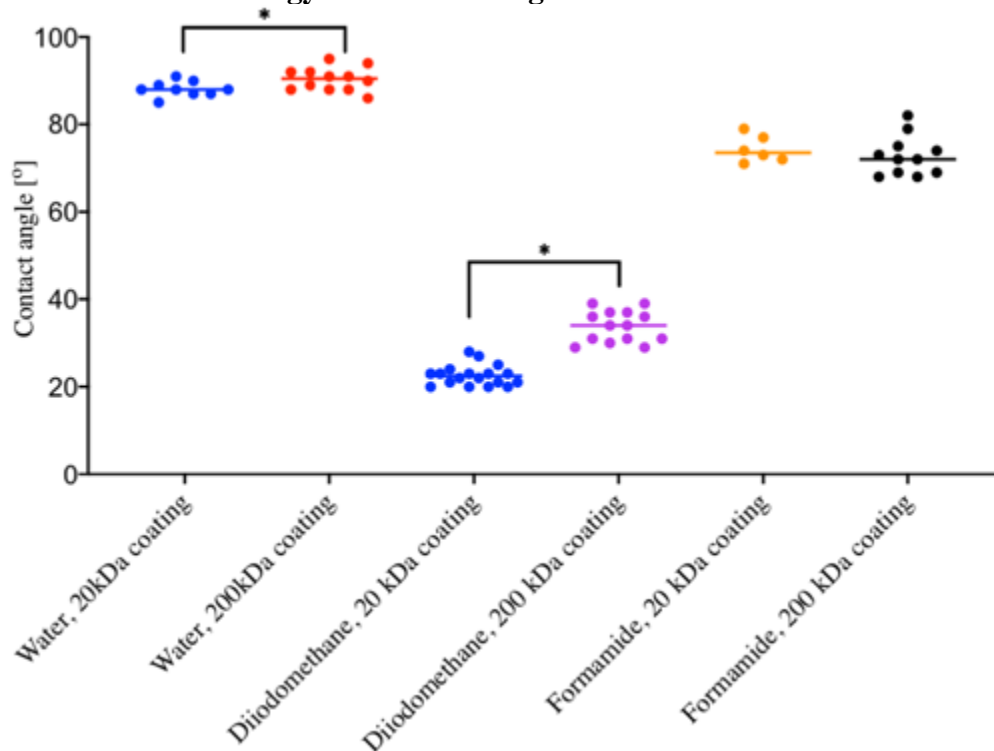


Fig. S13. Contact angle of water, diiodomethane and formamide on 20 kDa and 200 kDa coatings. * - means are significantly different, t test ($p < 0.05$). (GraphPad Prism 9, <https://www.graphpad.com/scientific-software/prism/>)

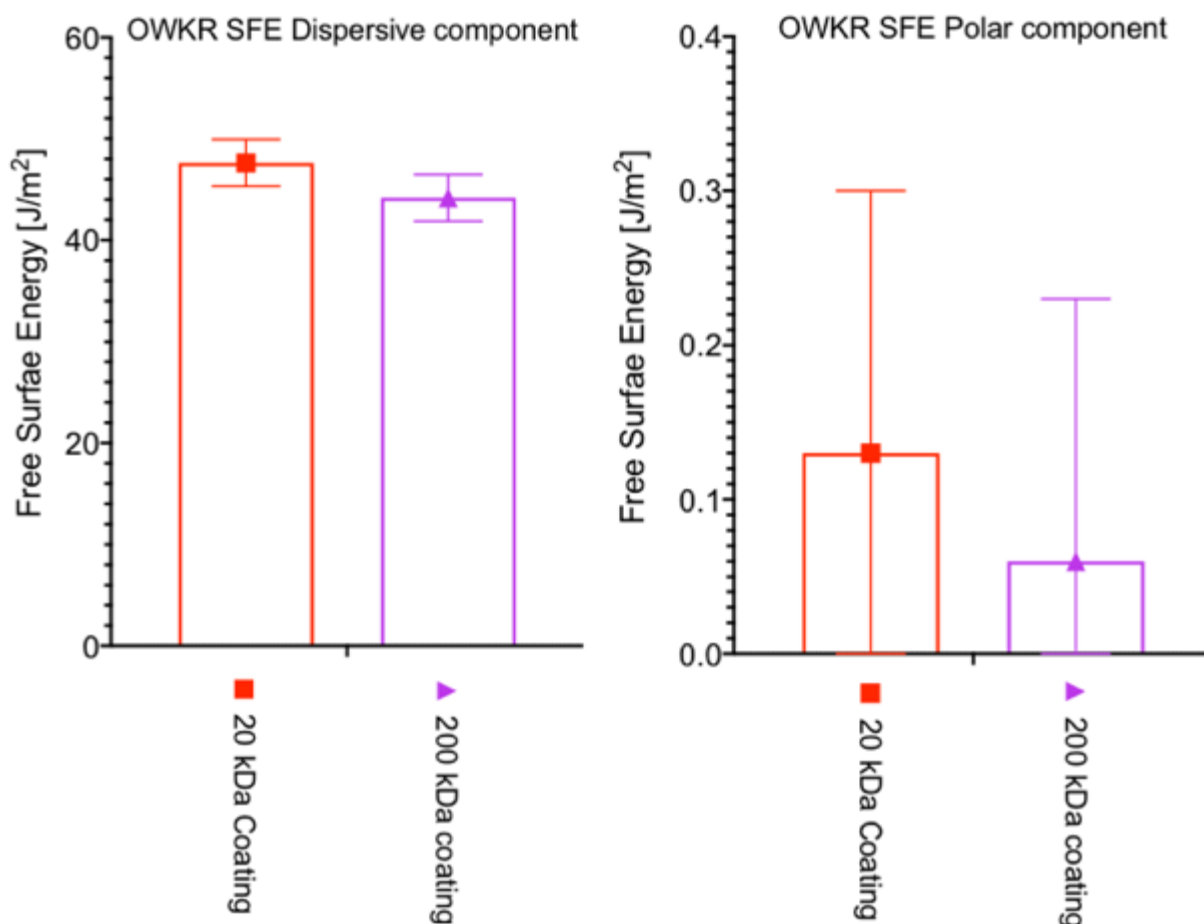


Fig. S14. Free Surface Energy of 20 kDa coating and 200 kDa coating, OWKR Method.[5] (GraphPad Prism 9, <https://www.graphpad.com/scientific-software/prism/>)

8. Varying the spin-coating time

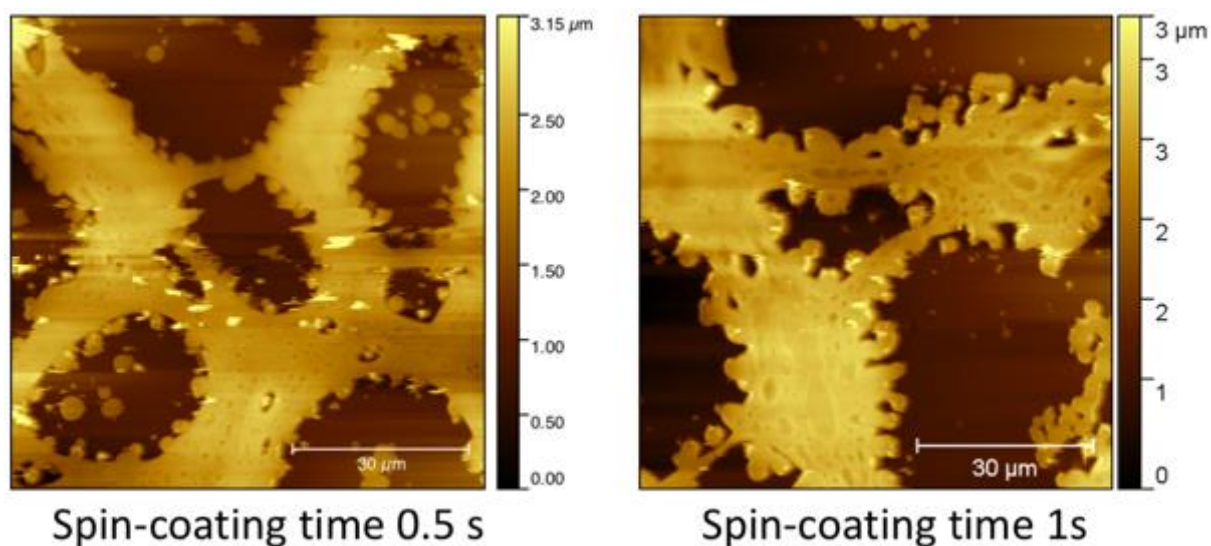


Fig. S15. PS 20 kDa and 200 kDa blend, 75/25 ratio, Spin-coating time: 0.5s and 1s. (Gwyddion v2.50, <http://gwyddion.net>)

References:

- [1] Morgan Stefik, "Spincoater," 2018. [Online]. Available: <http://www.stefikgroup.com/spin-coater/>.
- [2] C. Huang, "Phase Separation in Thin Polymer Films : From Self Stratification to Polymer Blend Lithography," no. August 2014.
- [3] D. T. W. Toolan, " Straightforward technique for in situ imaging of spin-coated thin films ," *Opt. Eng.*, vol. 54, no. 2, p. 024109, 2015, doi: 10.1117/1.oe.54.2.024109.
- [4] C. Y. Liang, S. Krimm, S. M. Barber-Meyer, L. D. MeCh, C. Y. Liang, and S. Krimm, "Infrared spectra of high polymers. VI. Polystyrene," *J. Polym. Sci.*, vol. 27, no. 115, pp. 241–254, 1958, doi: doi:10.1002/pol.1958.1202711520.
- [5] J. W. Drelich, "Contact angles: From past mistakes to new developments through liquid-solid adhesion measurements," *Adv. Colloid Interface Sci.*, vol. 267, pp. 1–14, 2019, doi: 10.1016/j.cis.2019.02.002.

Supporting_information_may21.pdf (1.85 MiB)

[view on ChemRxiv](#) • [download file](#)
